УДК 550.385 DOI: https://doi.org/10.24028/gj.v46i6.307063

Induction arrow spatial and temporal variations

I.I. Rokityansky, A.V. Tereshyn, 2024

S.I. Subbotin Institute of Geophysics of the National Academy
of Sciences of Ukraine, Kyiv, Ukraine
Received 27 June 2024

The induction arrow **C** is a characteristic of the variable geomagnetic field at one observation point (x, y) for a certain period T of geomagnetic variations **B**. It visually describes the magnitude and direction of the deviation of the geomagnetic field vector from the horizontal plane. The induction arrow is nonzero only when the vertical component B_z appears. B_z appears in three cases: 1) electrical conductivity's horizontal gradients under the surface of the globe; 2) incomplete compensation of the vertical component of the primary field of the ionosphere-magnetosphere source by the secondary field induced in the horizontally layered Earth. The degree of compensation systematically changes during the day, year..., leading to temporal variations in the induction arrow (source effect); 3) the appearance of not-removed noise or lithosphere emission containing B_z. This article presents the spatial and temporal variations of the induction arrows. Real (in-phase) and imaginary (out-of-phase) induction arrows (vertical response functions or tippers) were obtained for every day with proper observations from 1991 to 2014 years for five intervals of periods: 150—300 s, 300—600 s, 600—1200 s, 1200—2400 s, 2400—3600 s, calculated from three components of geomagnetic field recorded at 137 observatories of the global network INTERMAGNET. To reduce the scatter, the daily values were recalculated to monthly values. Such global material from +87° to –88° of geomagnetic latitude was obtained for the first time and its analysis yielded new scientific results. The annual variations (with a period one year) are visible at about 2/3 of the observatories (at the other observatories, they are below the background level of shorter period variations and/or noise). Its amplitude strongly depends on the geomagnetic latitude and sometimes reaches such a high value as 0.4—0.5 (peak-to-peak) at high (>65°) latitudes and varies within 0.01—0.15 at middle and low latitudes. Previous studies at middle latitudes discovered that the annual variations in the northern component A_u is positive everywhere (maximum in June, minimum in December) and proposed, as a global source model for the annual variations explanation, the ring current at the height 3—6 Earth's radii. We discovered that at high latitudes, A_u is usually negative. We propose to explain all the observed features of the induction arrow's annual variations by variations of the ionosphere currents in the aurora zone. 11-year variations are found at ≈30 % of observatories located at all latitudes but more frequently in aurora zones. At a few observatories, trends (monotonous changes in arrows) were found. The largest trend of magnitude 0.2 for all periods was found in southern Greenland, where glaciers have been melting rapidly over the past 30 years, which makes it possible to associate both trends with global warming. In a few aurora observatories of North America trends of magnitude ≈0.1 were noticed. In these same years, the North Magnetic Pole unusually rapidly migrated for 1100 km in 23 years. It can be assumed that these trends are related to changes in the aurora oval position. At geomagnetic latitudes from –78° to +78°, the main harmonic (24 hours=86400 s) of daily variations of the geomagnetic field is always accompanied by at least one higher order harmonic 24/n (n=1÷7).

Citation: Rokityansky, I.I., & Tereshyn, A.V. (2024). Induction arrow spatial and temporal variations. *Geofizychnyi Zhurnal*, *46*(6), 3—40. https://doi.org/10.24028/gj.v46i6.307063.

At higher latitudes >78° of both hemispheres only the fundamental 24-hour harmonic is visible. Induction arrow temporal variations create difficulties in determining its constant component used to study the electrical conductivity of the Earth's crust and upper mantle but can be very useful for geodynamic processes study.

Key words: electrical properties, electromagnetic theory, geomagnetic induction, magnetotellurics, time-series analysis.

Introduction. Electrical conductivity $\sigma(\mathbf{r})$ is a physical parameter used to study solid Earth composition, structure, and physical state. The deep Geoelectrics using natural ectromagnetic (EM) fields of magnetosphere-ionosphere origin includes three methods:

– GDS — geomagnetic deep sounding. Source — spatial harmonics of the geomagnetic field, studied model — 1D concentrically layered Earth;

– MTS — magnetotelluric sounding. Source — vertically incident horizontally uniform electromagnetic field, studied model — 1D horizontally layered Earth. It is the Tikhonov-Cagniard (T-C) model;

– MVP — magnetic variation profiling. Source — vertically incident horizontally uniform geomagnetic field, studied model — 2D and 3D anomalies of electrical conductivity that is the strong deflections of the conductivity from the 1D horizontally layered Earth.

Of course, all three methods work with the same complex natural external EM-field on the same complexly constructed Earth. The above field sources and earth models show those approximations for which basic mathematical models of each method are created for their operation. Given that in the MTS-method, deviations of real models from idealized ones are observed both in magnetic and electric fields but in the MVP-method, deviations are observed only in magnetic fields, it is much easier to detect these deviations in MVP than in MTS. Therefore, the MVP-data are much easier to clean and obtain reliable, although not very detailed, results on the location and parameters of the electrical conductivity anomalies.

Methodology. ***Response function (RF).*** The term «Response function» in geoelectromagnetic studies has a clear physical meaning: it is a reaction, an answer of the object of the study (Earth's conductivity structure) to the action of external EM-field variations. This response carries information on the conductivity structure. Observed magnetic fields also contain this response (useful information) and a great amount of excessive information about the sources of all types (external EM, internal lithosphere emission, and near-the-surface noise). To get rid of the excess information (about the sources), we transfer data from the geomagnetic field to the RF of the real Earth at an observation point (profile, area).

Thus, the RFs are supposed to be some functions derived from the Earth's (electro) magnetic field that allow us to facilitate the conductivity structure determination. EM RFs are usually frequency/(period T) dependent, and then they are complex functions having real (index u) and imaginary (index v) parts. The main RFs in MTS are impedance and apparent resistivity; in MVP — induction arrow or tipper and horizontal magnetic tensor M. We use in this study mostly the induction arrow.

Geomagnetic field presentation. The geomagnetic variation field of the magnetosphere-ionosphere origin can be represented as the sum of three main parts: the primary external field — $\mathbf{B}_{0e}$ of the currents in the magnetosphere and ionosphere, the secondary normal internal field — $\mathbf{B}_{0i}$ due to the currents induced in a layered 1D Earth and the secondary anomalous field — $\mathbf{B}_a$. If the conductivity anomaly dimensions are much less than the source's dimensions, it can be assumed that the anomaly-forming field will be $\mathbf{B}_0=\mathbf{B}_{0e}+\mathbf{B}_{0i}$. Then, the anomalous currents and fields depend linearly on the normal field strength that can be expressed by the three-dimensional tensor [Schmucker, 1964, 1970]:

$$\mathbf{B}_a(x,y)=\left[b_{ik}(x,y)\right]\mathbf{B}_0(x,y), \qquad (1)$$

which can be expanded into three components

$$B_{xa} = b_{11}B_{x0} + b_{12}B_{y0} + b_{13}B_{z0}\,, \qquad (2)$$

$$B_{ya} = b_{21}B_{x0} + b_{22}B_{y0} + b_{23}B_{z0}\,, \qquad (3)$$

$$B_{za} = b_{31}B_{x0} + b_{32}B_{y0} + b_{33}B_{z0}\,. \qquad (4)$$

The induction arrow is defined as follows

$$\mathbf{C} = A\mathbf{e}_x + B\mathbf{e}_y\,, \qquad (5),$$

where $\mathbf{e}_x$ and $\mathbf{e}_y$ are unit vectors in the North and East directions; A and B are determined from the system of linear equations:

$$B_z = AB_x + BB_y\,. \qquad (6)$$

The minimum number of terms in Eq. (6) is two, presented by variations with different polarization of the horizontal field (in order for the system's determinant to be not zero). In practice, all available records are used for processing and the most probable values of A and B are calculated using statistical methods to assess their statistical error. Eq. (6) is similar to Eq. (4) (neglecting B_{z0}), but instead of the anomaly-forming normal horizontal field $\mathbf{B}_0$ in Eq. 4 stands the total horizontal field: normal+anomalous:

$$B_x = B_{x0} + B_{xa} =$$
$$= B_{x0}\left[1 + b_{11} + \left(B_{y0}/B_{x0}\right)b_{12}\right], \qquad (7)$$

$$B_y = B_{y0} + B_{ya} =$$
$$= B_{y0}\left[1 + b_{22} + \left(B_{x0}/B_{y0}\right)b_{21}\right]. \qquad (8)$$

The solution of (6) can be presented as follows:

$$A = b_{31}\Big/\left[1 + b_{11} + \left(B_{y0}/B_{x0}\right)b_{12}\right], \qquad (9)$$

$$B = b_{32}\Big/\left[1 + b_{22} + \left(B_{x0}/B_{y0}\right)b_{21}\right]. \qquad (10)$$

When using observations at one point, the normalization of the anomalous field in the vertical component is done not with respect to the anomaly-forming normal horizontal field $\mathbf{B}_0$, but to the total horizontal field. The last term in the denominators of Eqs. (9, 10) depends on the normal field polarization, in which variations cannot be detected by one-point observations. It can cause an error, especially large in the epicenter zone of the anomaly where the horizontal field anomaly is maximal (Fig. 1): on many anomalies it approaches 1, and on some of them it exceeds 1. In the epicenter zone, the error can reach a few tens of percents, and it can manifest itself both as a data scatter and as a systematic error, which explains the unstable behavior of the induction arrows observed over and near the anomaly axis.

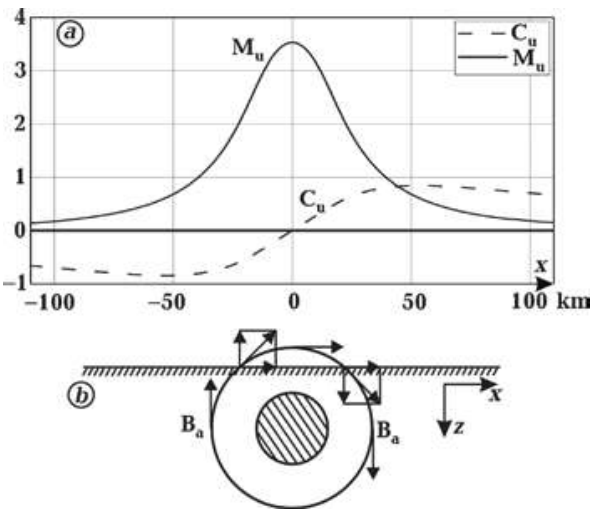

Fig. 1. Formation of anomalous magnetic fields over a two-dimensional conductor: *a* — profile plots of the real (in-phase, index u) anomalous fields with appropriate normalization: horizontal $M_u=b_{xa}=B_{xa}/B_{x0}$ — solid curve and vertical response function $C_u=B_{za}/(B_{x0}+B_{xa})$ — dashed line. The increase of electrical conductivity with depth (NGCS) reduces the Earth's impedance and the anomaly-forming normal fields $\mathbf{E}_0$ and $\mathbf{B}_0$ and, consequently, the anomalous fields. NGCS used in calculations is presented in Table; *b* — an anomalously conducting cylinder (ρ_i=1 Ohm·m, radius=15 km, depth of the center=25 km) embedded in the upper layer (thickness=100 km, ρ_e=1000 Ohm·m) of the Normal Geoelectric Cross-Section (NGCS) (see Table below) and a line of force of the anomalous magnetic field around the conductor, decomposed into horizontal and vertical components.

Spatial and spectral properties of the induction arrows. Figs. 1—3 illustrate the above considerations by the calculations of horizontal anomalous field $M=[b_{ik}]$ (according to Eqs. (2, 3) at B_{z0}=0) and induction arrow $\mathbf{C}$ arising around a simple 2D model with the parameters typical for the large natural crustal conductivity anomalies. The real (in-phase) induction arrows $\mathbf{C}_u$ are given in the Wiese convention i.e., they are directed from high conducting anomaly. The imaginary vector $\mathbf{C}_v$

shown in Figs. 2—5 is parallel to C_u for short periods and anti-parallel for long ones (it is valid for exp(–*iωt*) time factor, for exp(+*iωt*) vice versa).

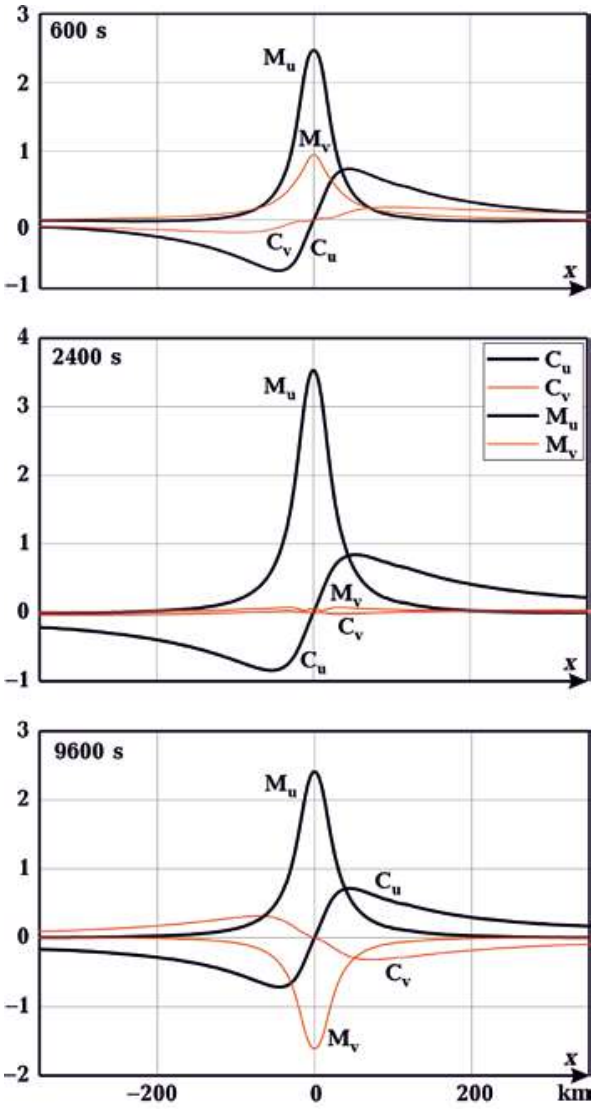

Fig. 2. Profile graphs for short (600 s), central (2400 s) and long (9600 s) periods. Index v denotes the imaginary (out-of-phase) values. The middle graph corresponds to the period T_0 at which the amplitude of the real anomalous field is maximal and the imaginary one passes through zero changing sign (see Fig. 3).

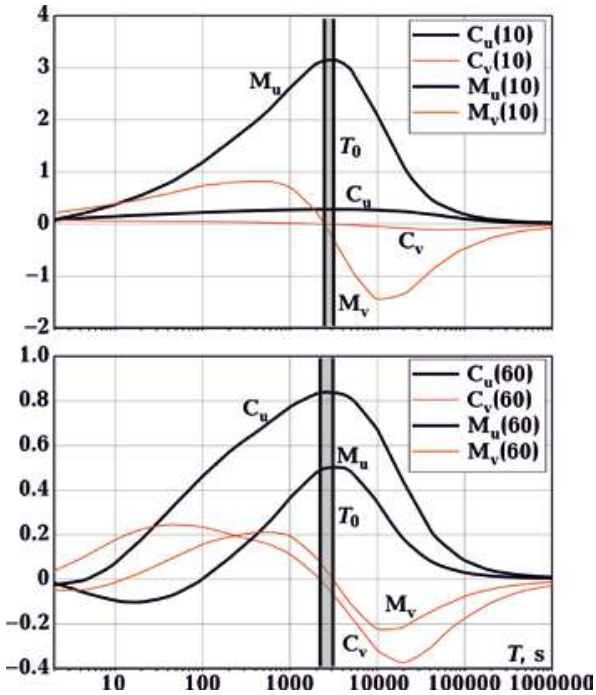

Fig. 3. Spectrum (frequency characteristic) of the anomalous fields calculated for the 2D electrical conductivity anomaly described in Fig. 1. T_0 — spectral line (more precise — stripe) of the anomaly, closely associated with its longwise conductance $G=Q\cdot\sigma_i$, where Q is the cross-sectional area of the anomaly, σ_i — its conductivity. The upper graph represents the spectrum at the point x=10 km, where the horizontal component is close to its maximum value, and the lower one, at the point x=60 km, where **C** is close to its maximum.

In Donbas in an earlier study [Rokityansky et al., 1989], the anomalous fields were normalized to carefully selected observatory with normal field B_{x0}. Over the anomaly axis, sites NNG and DYAK, (see Fig. 4) the horizontal component b_{xa} attains value 3, and the vertical b_{za} is <0.3. The vertical component b_{za} attains a maximum value of 2 at the distance 45 km from the anomaly axis at the site PYAT where b_{xa}=0.3. The induction arrow $\mathbf{C}_u$ in the same site PYAT has a value of only 1.6 because one site processing normalizes B_{za} to $B_{x0}+B_{xa}$ as was described above in Eq. (7).

Simplified 1D Normal Geoelectric Cross-Section compiled by data [Rokityansky, 1982, Table 16] — mainly continental observatory data and [Kuvshinov et al., 2021, Table 1, Fig. 7] — global both satellite and observatory data

Depth interval, km	0—100	100—200	200—400	400—600	600—800	>800
ρ, Ohm·m	1000	600	200	10	3	1

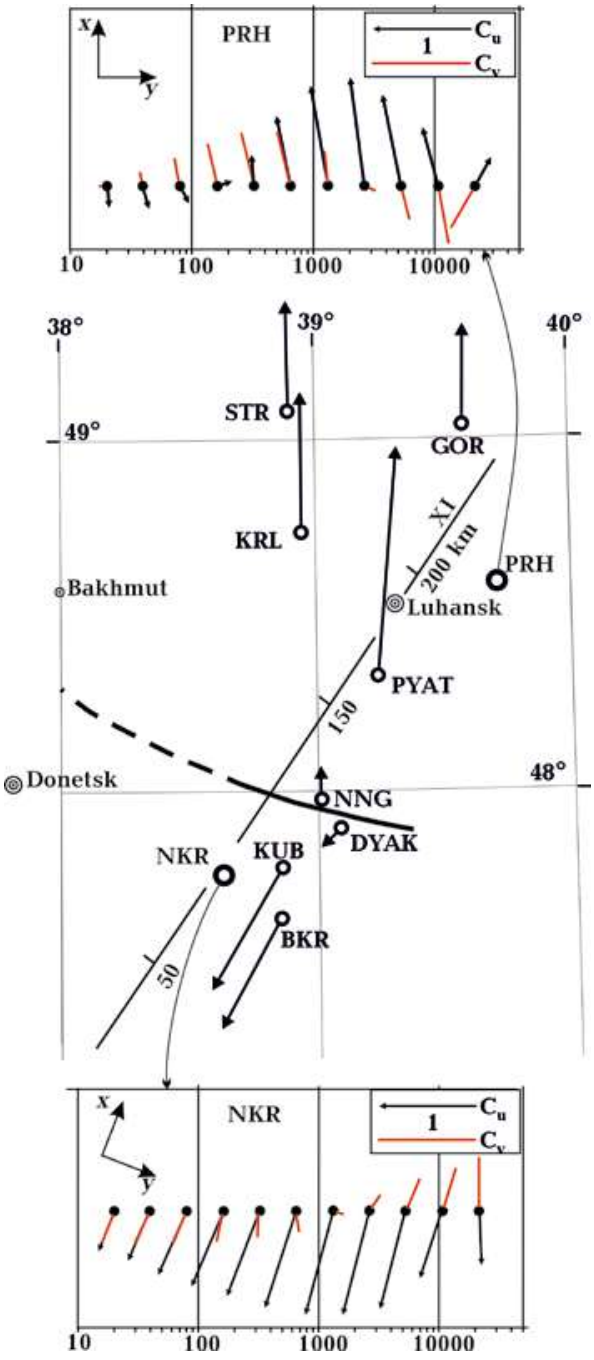

Fig. 4. Practical example. Induction arrows on the Donbas electrical conductivity anomaly are given for the period interval 1800—5400 s at which the anomalous fields are maximal. Anomaly axis is shown by thick line. Straightline XI across the anomaly is the DSS profile. The induction arrows are obtained from observations with old analog torsion magnetometers [Rokityansky et al., 1989]. In the upper and lower blocks of the Figure, the results of recent digital observation are given for two sites shown on the map by circles. The directions *x* and y are chosen not to be the same at these two sites, but so that *x* coincides with the direction of the arrows in each area.

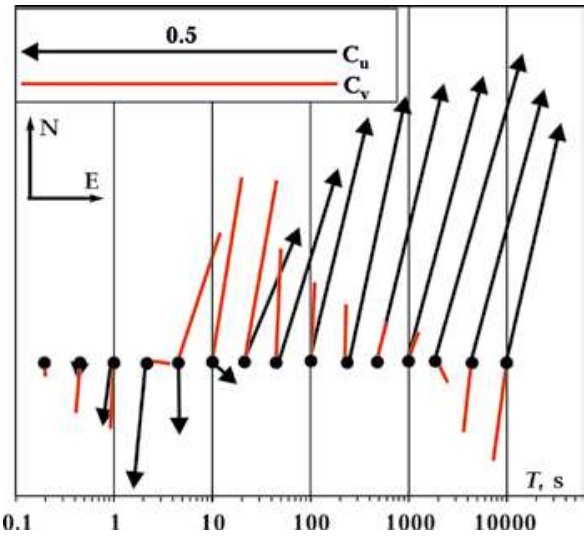

Fig. 5. The induction arrows for periods 0.1—10000 s at observatory GAN in the Maldives built for the data calculated in [Rigaud et al., 2021]. The sign of the $\mathbf{C}_v$ is reversed to our time factor $\exp(-i\omega t)$.

Consider the induction arrows obtained in a wide frequency range (sites NKR and PRH in Fig. 4). The origin of the profile plots (of the *x*-axis) is over the anomaly axis. Site NKR is located 30 km southward from the axis and $\mathbf{C}_u$ has a negative sign (exactly as in Figs. 1, 2 at $x<0$). Site PRH is located 85 km northward from the axis of main anomaly and $\mathbf{C}_u$ has positive sign. On the frequency graphs, the origin of coordinates is not defined; the position T_0 of the maximum of the real part of the anomalous field is usually taken as the center of the graph. Consider the spectrum in NKR. Maximum $\mathbf{C}_u$ is observed at $T_0 \approx 1800$ s, $\mathbf{C}_v$ at shorter periods is parallel with $\mathbf{C}_u$ and arrives at the same value as $\mathbf{C}_u$ at the shortest periods. At periods longer than T_0, $\mathbf{C}_v$ is antiparallel to $\mathbf{C}_u$ and both diminish more rapidly than at short periods (because at long periods the deep well conducting layers of the normal cross-section reduce the normal field stronger than at short periods). Exactly the same we see on theoretical curves of Fig. 3. At site PRH, central and long-period parts of the spectrum are very similar to NKR, which is natural for the field of the same electrical conductivity anomaly. At short periods at PRH there appears, one more anomaly of a smaller scale with $T_0 \approx 20$ s approximately parallel to

a large scale Donbas anomaly but with the opposite sign because this smaller anomalous conductor is located northward from the PRH site. It is a well-known shallow conductor in sediments.

A similar interaction of two different-scale anomalies is presented in [Rigaud et al., 2021]. The authors processed the geomagnetic variations recorded at 11 low-latitude (±37°) oceanic island observatories and obtained induction arrows in the 300—10000 s range. With detailed data on seafloor bathymetry and seawater conductivity, they calculated (direct problem) tippers in the range 0.1—10000 s. The induction arrows spectrum at observatory GAN presented in Fig. 5 contains two spectral lines at $T_0 \approx 3$ s and 3000 s whose sources can be interpreted as two independent conductors with very different longwise conductance G.

Short discussion. It can be seen from the presented graphs that three zones can be distinguished around the compact isometric long (quasi-2D) anomaly according to the behavior of the induction arrows. Above the axis of the anomaly, the arrows are small, change rapidly and are not stable. In the middle zone, the arrows are maximum (>0.3), stable, and cover a wide spatial band. They form the basis for determining the parameters of the anomaly. In the outer zone, where the amplitude of the arrow is reduced, superposition from other distant anomalies is often observed. With a sparse network of observatories, like the INTERMAGNET, it is not easy to understand the situation in the outer zone.

For coastal observatories, the anomalous fields have an obvious source. It is the coast effect, which occurs due to the contrast in the electrical conductivity of land and seawater. Conductivity anomaly (sea-water) is usually asymmetric. The transition from land to ocean depths usually goes through three steps: coastal shallows 3—30 m deep, shelf ≈200 m deep and ocean depths 4—5 km. Each of these anomalous formations, being a separate structure with a rectangular cross-section, would have anomalous fields (and induction arrows) with a maximum on the period T_0 equal to about 1—4 s for coastal shallows, ≈50 s for shelf and 2000—3000 s for deep ocean. In some coastal or island observatories (see Fig. 5), two separate T_0 maxima can be observed. For this, the observed and processed data must contain variations with the period's interval no less than two orders wide. Our INTERMAGNET data processing covers the interval of only 150—3600 s, which is hardly enough to observe two T_0 maxima. However, one T_0 maximum is also an interesting result which will be presented for several observatories.

Processing and analysis of its results. ***Processing technique.*** The processing of the data recorded in the time interval ΔT (usually one day in this work) is a transformation from three synchronous time series B_x, B_y, B_z of the geomagnetic field components with a discreteness Δt (1 min — data INTERMAGNET) into the time series of the induction arrow components A_u, B_u, A_v, B_v for the set of selected periods T_n (T_1=225 s, T_2=450 s, T_3=900 s, T_4=1800 s, T_5=3000 s) with discreteness ΔT=1 day. Obviously, $\Delta t << T_n << \Delta T$.

Processing was carried out using the [Klymkovych, 2009] program and the PRC-MTMV research program [Varentsov et al., 2003; Varentsov, 2007]. Both are based on a high-resolution fast Fourier transform, calculation of cross- and auto-correlation energy spectra between magnetic field components, and subsequent partial estimator procedure in a set of overlapping windows, and a multistage selection of acceptable estimators according to coherence criteria. The Varentsov program is multifunctional and provides a solution to a wide range of problems. The program participated in several international projects such as BEAR, EMTESZ-Pomerania, and others, and obtained the best results. The Klymkovych program is specially designed to calculate induction arrow. It has been used for 20 years to monitor earthquake precursors in the Carpathians. The program operated with a fixed set of coherency criteria (Coh2IN ≤ 0.5, Coh2Multy ≥ 0.6) to ensure uniformity and consistency in processing results at all observatories.

Recall that the input coherency is calculated between horizontal components B_x and B_y and its small value (coh2IN < 0.5) indicates

a rich set of polarizations of the primary MT-field, which is necessary for the proper resolution of the induction arrow components. Multiple coherence between B_z and (B_x, B_y) characterizes the quality of the linear relationship $B_z=AB_x+BB_y$, and its high value (coh-2Multy > 0.6) is necessary for the stable calculation of the induction arrow.

For the studied periods from 225 to 3000 s, coherence conditions are generally satisfactory for the middle-latitude observatories and somewhat worse for some high-latitude observatories characterized by higher uncertainty. For 32 observatories of the North America region, coherences are presented in Appendix D. They are calculated for intervals 1 year long and show the mean coherences of the geomagnetic field during this interval. In some observatories, the mean values are below the threshold level.

Nevertheless, our processing program with incorporated coherency-based criteria thresholds usually finds time intervals for calculating the induction arrow's components with acceptable uncertainty. If adequate time intervals were not found, a day was excluded from the dataset. Only robust results were used.

Selection of optimal averaging. To select the averaging interval for the presentation of global data, consider three North America observatories (Fig. 6). The statistical uncertainty of the everyday processing and average monthly estimate was 0.06 and 0.011 in THL, 0.055 and 0.01 in SIT, and 0.022 and 0.004 in FRD. The observed scatter is much larger (the same is observed in the graphs in [Araya, Ritter, 2016]). However, despite the scatter, the annual variation at all three observatories and the 11-year variation in SIT can be seen in the daily records. However, these variations are seen much better in the monthly averaged curves. Hereafter we will operate mainly with monthly average values. This ruled out the study of variations shorter than three months, but the remaining material is still so voluminous that only some fragments can be shown.

Uncertainties. Uncertainties were calculated for all processed observatories. They strongly depend on the observatory's geomagnetic latitude. The North America region is well represented by different geomagnetic latitudes and it was chosen to show uncertainties (Fig. 7).

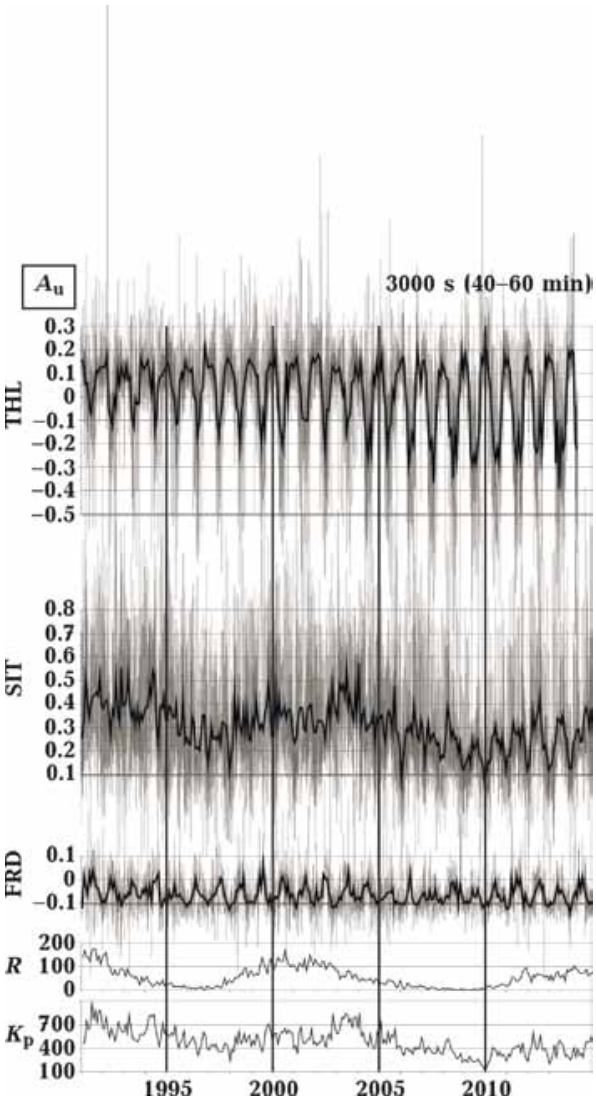

Fig. 6. Time variations A_u at three observatories in North America: THL (geomagnetic latitude 83.31°), SIT (60.19°), and FRD (47.95°). Every-day processed results are given in grey, and monthly averaged values are in black. R is the index of solar activity (Wolf number), and K_p is the monthly sum of the planetary index of geomagnetic activity.

The error in the RF calculation strongly depends on the geomagnetic field structure which is different for separate geomagnetic latitudes. The most heterogeneous and changeable field is observed in the aurora zone. The worldwide study showed that the

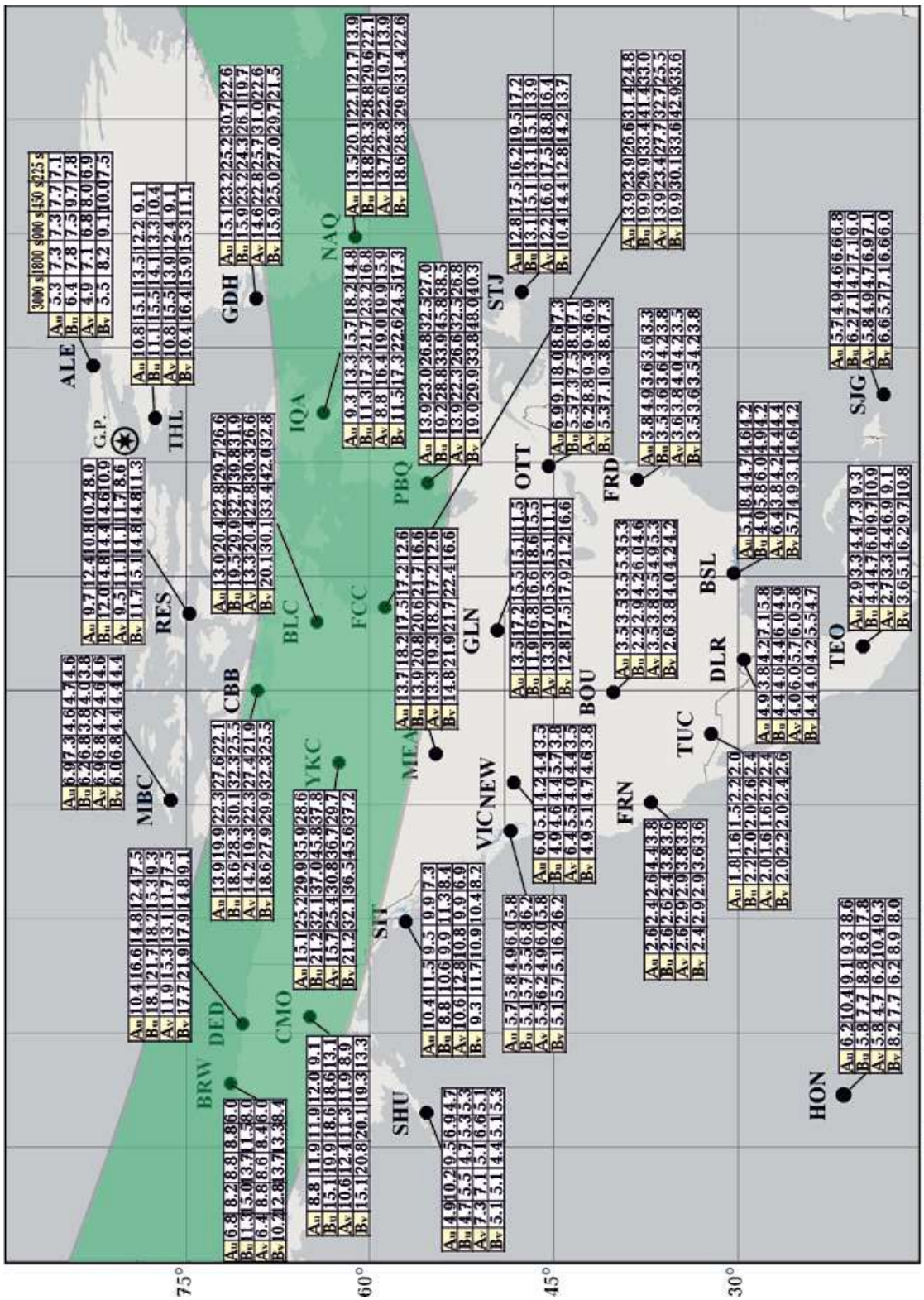

Fig. 7. Mean for all processed years Error (×1000) of monthly averaged components of induction arrow for five periods: 3000 s (left columns), 1800, 900, 450 and 225 s as shown for ALE observatory. The shaded stripe is the aurora zone, and the small star inside the circle is the geomagnetic pole (G.P.) for the epoch 2000—2010.

average statistical uncertainty of monthly average data in the aurora zone is 0.02—0.04, near the boundaries of this zone and inside the polar cap 0.01—0.02, and at middle and low latitudes 0.003—0.01. As a rule, the studied variations of the induction arrows, are much larger than the given uncertainties. The intensity of geomagnetic variations at high latitudes in several times greater than at middle latitudes and the useful MT signal-to-noise ratio will be more favorable there. On the other hand, at high latitudes the field sources are more local and the T-C model is more violated. It can be seen by considering the records synchronously (Appendix B).

Results of the worldwide INTERMAGNET data processing. The INTERMAGNET network (www.intermagnet.org) has collected and kept digital three-component records of the geomagnetic field with 1-minute discreteness (reading time) since 1991. Initially, there were 39 geomagnetic observatories; later (until 2010), a hundred more observatories joined the INTERMAGNET network.

Description of the obtained data. Data from 137 observatories (see Table A1) from 1991 to 2014 were processed, and time series were obtained for four components of the induction arrow A_u, B_u, A_v and B_v for five intervals of periods 2.5—5, 5—10, 10—20, 20—40 and 40—60 min with a central period of 225, 450, 900, 1800 and 3000 s, respectively. The location of the observatories on the world map is shown in Fig. 8.

There is not enough space to present all observatories for all components at all periods. The time series of the induction arrow components for 23 years presented in the following materials:

– Fig. 9 — 25 observatories from all latitudes selected with clearly visible annual variations, all four components, period 1800 s (20—40 min), relative scale;
– Fig. 10 — all 32 observatories of the North America region, components A_u and B_u, period 1800 s (20—40 min), absolute scale;
– Appendix C — all 32 observatories of the North America region, all components, all periods together, colored, relative scale;
– article [Babak et al., 2017] — eight ob-

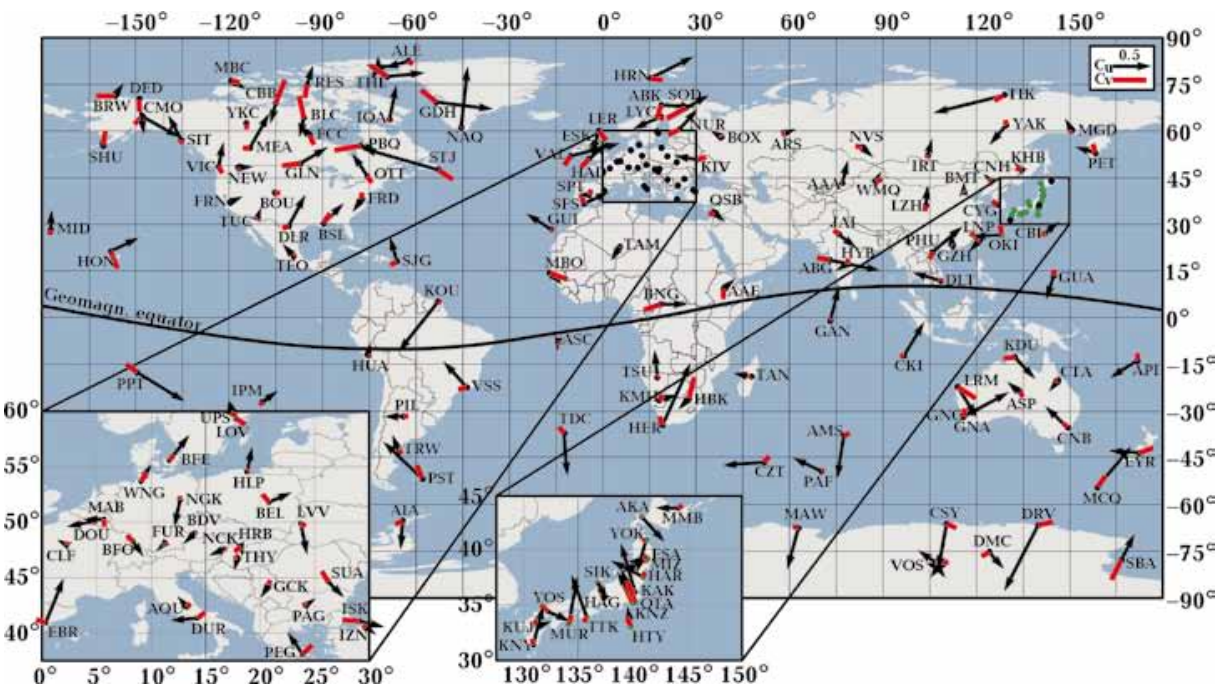

Fig. 8. 137 INTERMAGNET+14 Japanese observatories with real $\mathbf{C}_u$ and imaginary $\mathbf{C}_v$ induction arrows for period 1800 s (20—40 min), averages for the entire observation period presented for each observatory in Table A1. Geomagnetic poles for epoch 2000—2010 are marked by 5-ray stars.

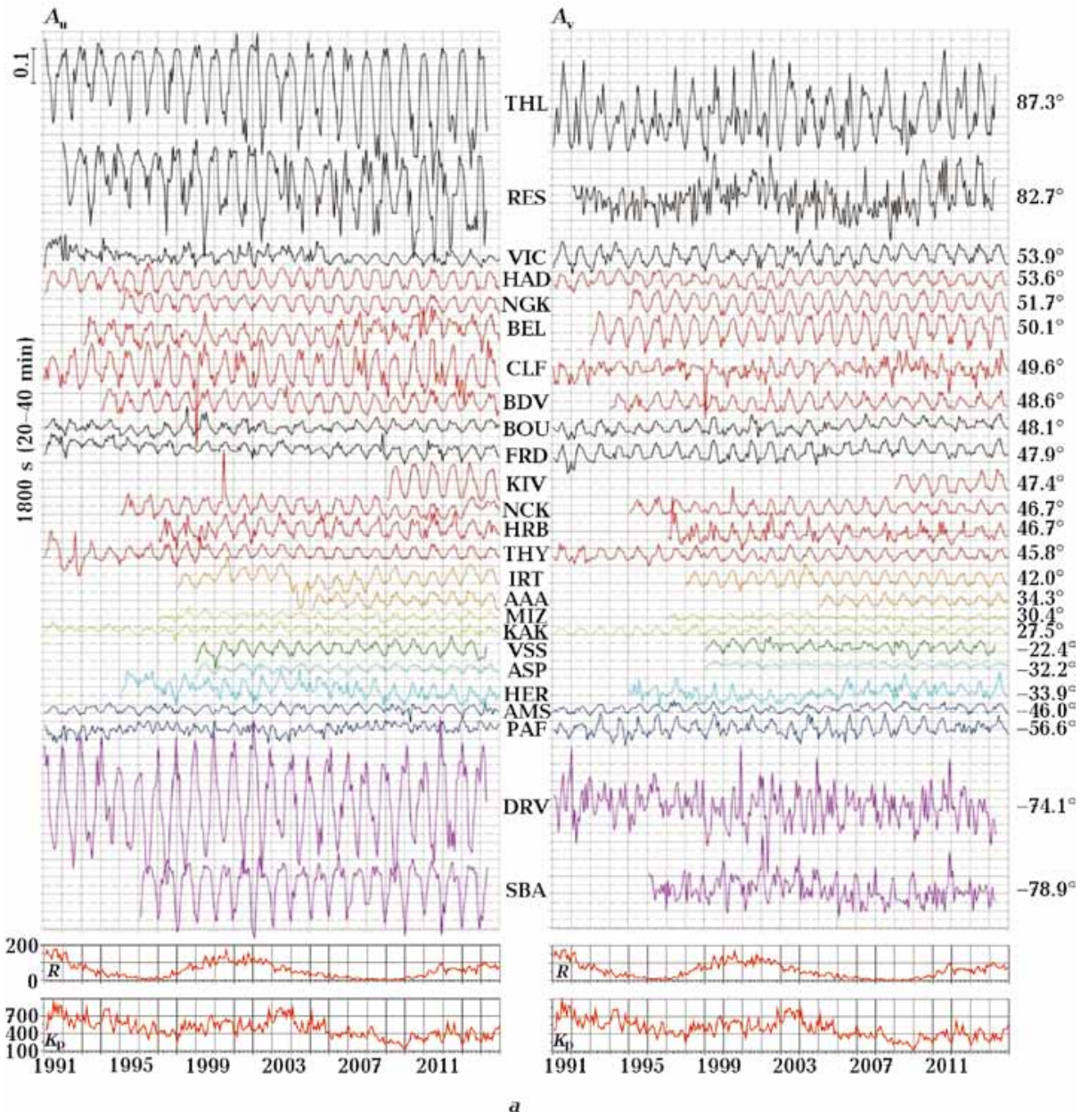

a

servatories from all latitudes, all components, periods 5—10 min, 10—20 min, 20—40 min and 40—60 min, absolute scale.

As follows from a careful examination of Fig. 10, over 23 years of observations at the INTERMAGNET observatories, no signals clearly associated with earthquakes were recorded.

Induction arrows behavior at selected observatories. THL (φ_m=87.31°) is located in northwest Greenland on the shore of the relatively deep (≈400 m) Smith Strait, which sea currents determine the eastward orientation of the real induction arrow with a gentle B_u maximum of 0.53 on periods of ≈5 min. This frequency characteristics corresponds to theoretical predictions for such sea depth [Rokityansky, 1982].

Variations of the induction arrow are given in various combinations in Fig. 9, 10. Annual variation (AV) is the most intense at the longest period of 3000 s, sometimes reaching a value of 0.5 on the A_u and B_v components. With the period decrease, the AV amplitudes gradually diminish in ≈3 times to values of the

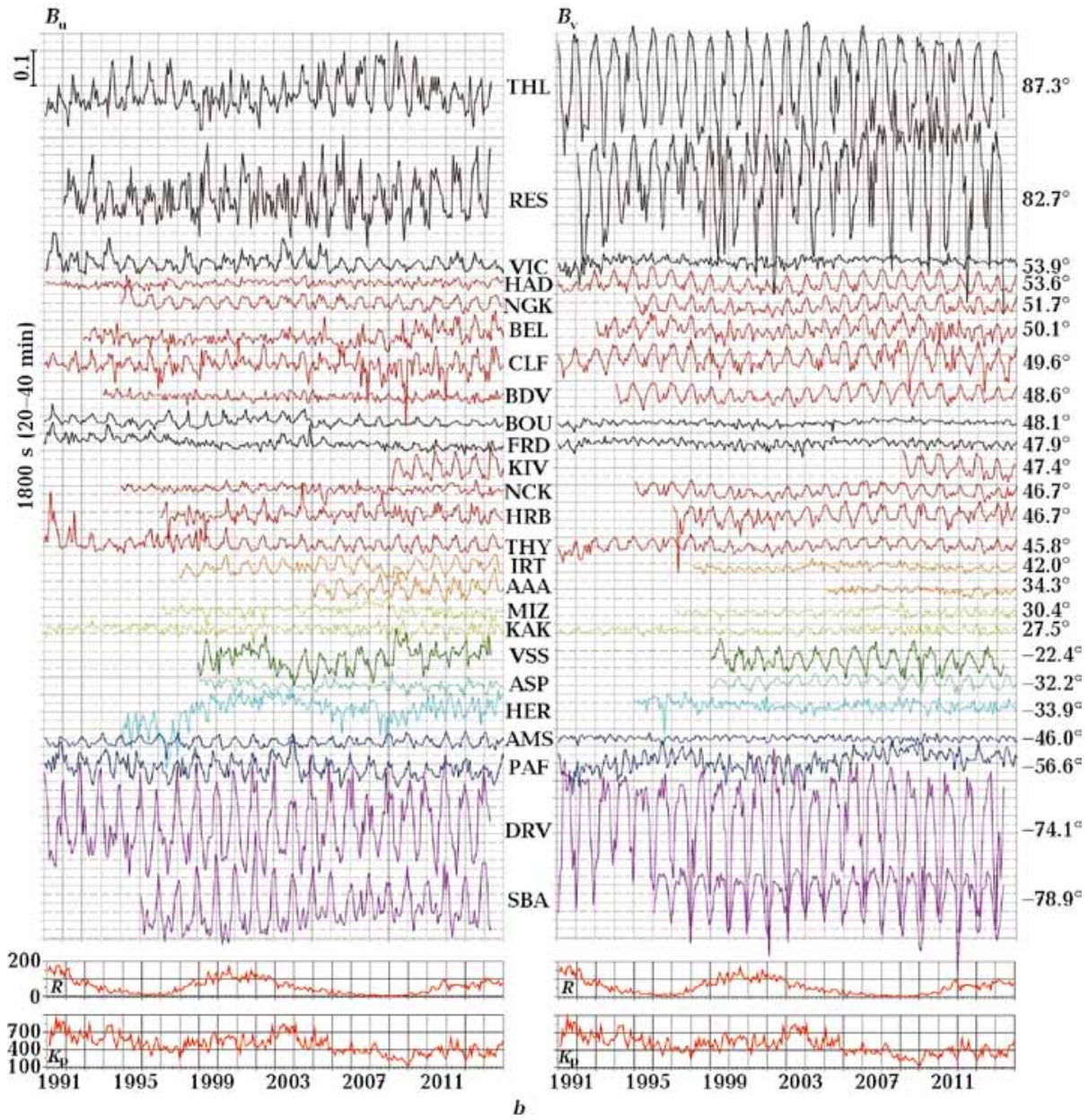

Fig. 9. Temporal variations of monthly average components of A_u and A_v, B_u and B_v in 1991—2014 for a period of 1800 s (20—40 min) at 25 observatories selected with clearly visible annual variations. The geomagnetic latitudes of each observatory are inscribed on the right. The scale for all observatories is the same; the level is not saved. The color of the curves depends on the location: black — North America, red — Europe, faded red — Asia, light green — Japan, green — South America, green-blue — Australia, blue — South Africa, dark blue — Indian Ocean, orange — Antarctica. R is the index of solar activity (Wolf number), and K_p is the monthly sum of the planetary index of geomagnetic activity.

order of 0.1. In A_u component, AV amplitude almost monotonously increased two-fold during 23 years at all periods. At other components, such monotonous change of AV amplitude is not observed. One exception: in the A_v component AV amplitude decreased two-fold at only two short periods during 23 years.

Strong AV modulation is observed in the B_u component at which AV amplitude during low solar activity of 1996 and 2007—2008 increased 1.5—2.5 times (depending on the period) compared with the years of high solar

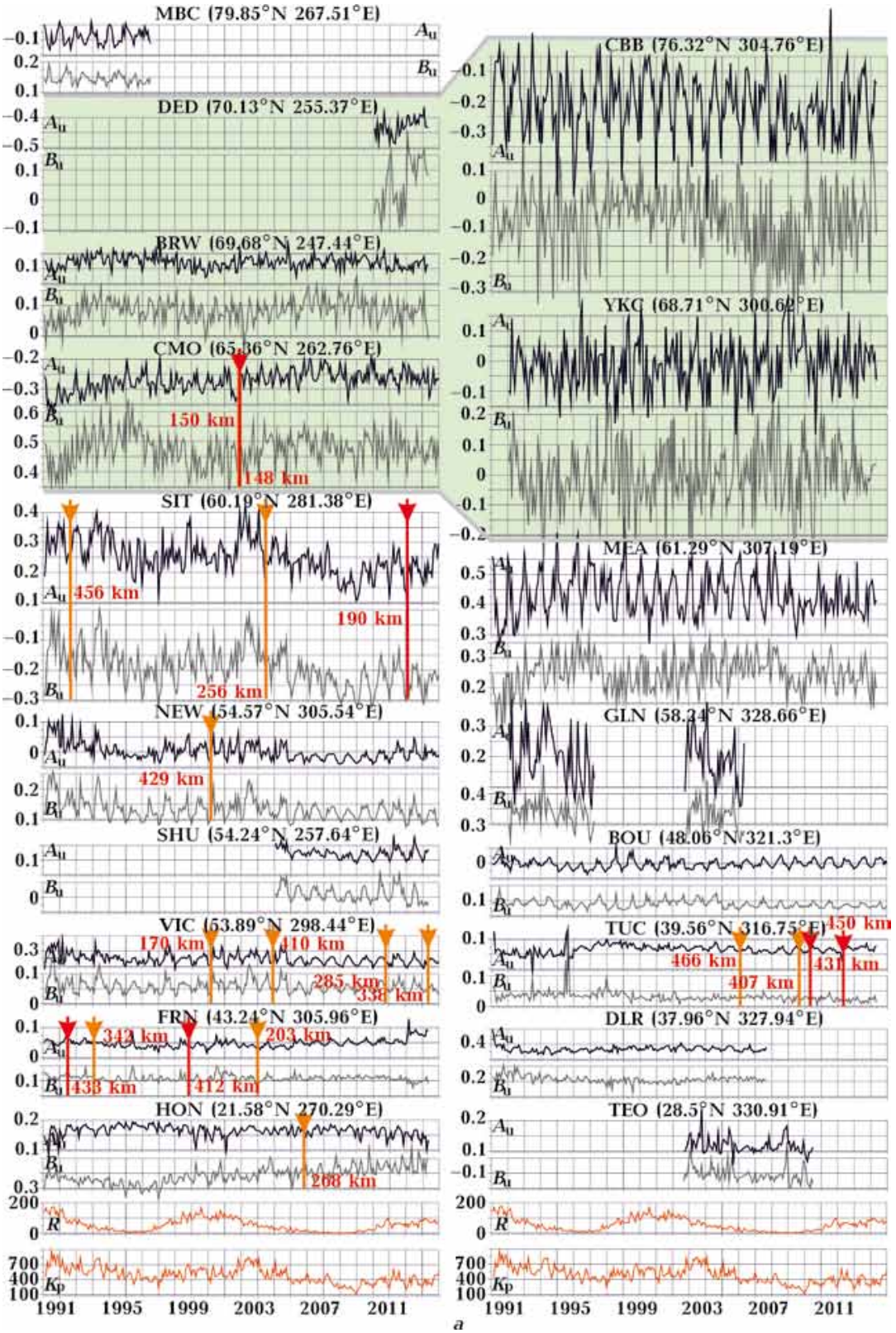

Fig. 10. Temporal variations of monthly mean values of induction arrow components A_u and B_u for the period 1800 s during 1991—2014 in North America region (see Fig. 7). Observatories disposed in four columns according geographical longitude and in every column according geomagnetic latitude. After each observatory code, geomagnetic coordinates for 2010-year epoch are given in brackets. The shaded background indicates the loca-

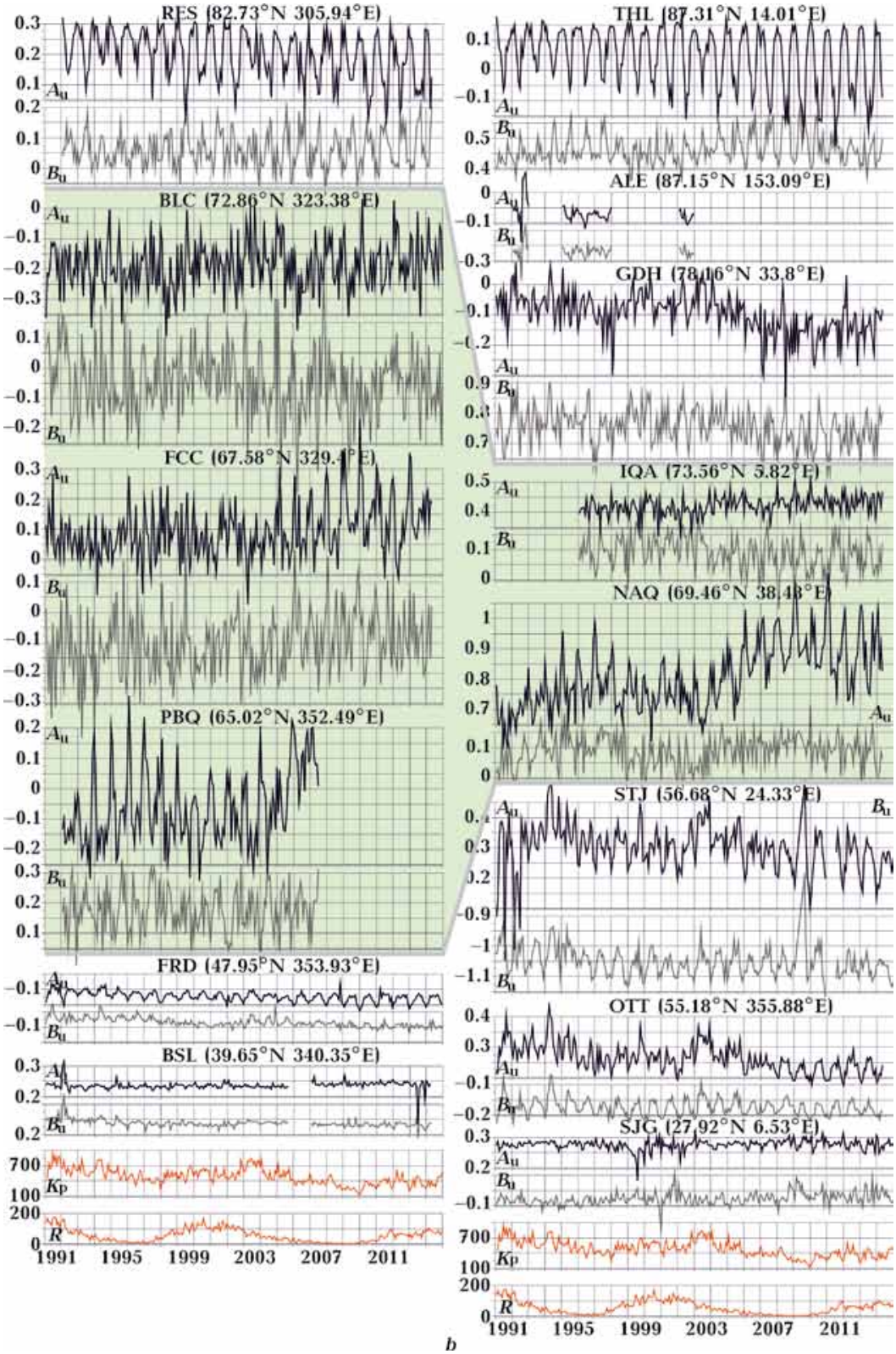

b

tion of the aurora zone (see Fig. 7). The western part of North America has high seismicity. We can expect seismic related anomalies at observatories of the first two columns, in which vertical lines with arrow mark the time of earthquakes (EQ) with magnitude M>6.5 occurred at a distance <500 km from observatory: the red line is for EQ of magnitude M>7, orange one — for M<7. R is the index of solar activity (Wolf number), and K_p is the monthly sum of the planetary index of geomagnetic activity.

activity. Such AV modulation can be considered as a part of solar cycle variation of the second kind (SCV-2). It is usually imposed on the simple 11-year variation (SCV). Typical SCV + SCV-2 are observed at the observatory GDH at A_v for short periods.

The sign of AV for A_u is negative at all periods: the blunted maximum in December—January is located at the same level for all years, the pointed minimum in June—July goes down, and the middle of AV slightly decreases showing at A_u a small trend of about 0.08 over 23 years for long periods and ≈0.03 for short ones.

ALE (φ_m=87.15°). One of the most interesting observatories is ALE, at which strong (up to three times) enhancement of horizontal field was recorded in the International Geophysical Year of 1957—1958. Alert anomaly was investigated in the 1960—1970s by several international teams [Law et al., 1963; Praus et al., 1971, etc.].

The authors oriented the magnetometers and earth current lines along and across the strike of the anomaly (NE and SE), which made it easy to interpret the observational data using the induction arrows, anomalies of the horizontal components, and apparent resistivity both separately and combined. Comparison of synchronous records of the

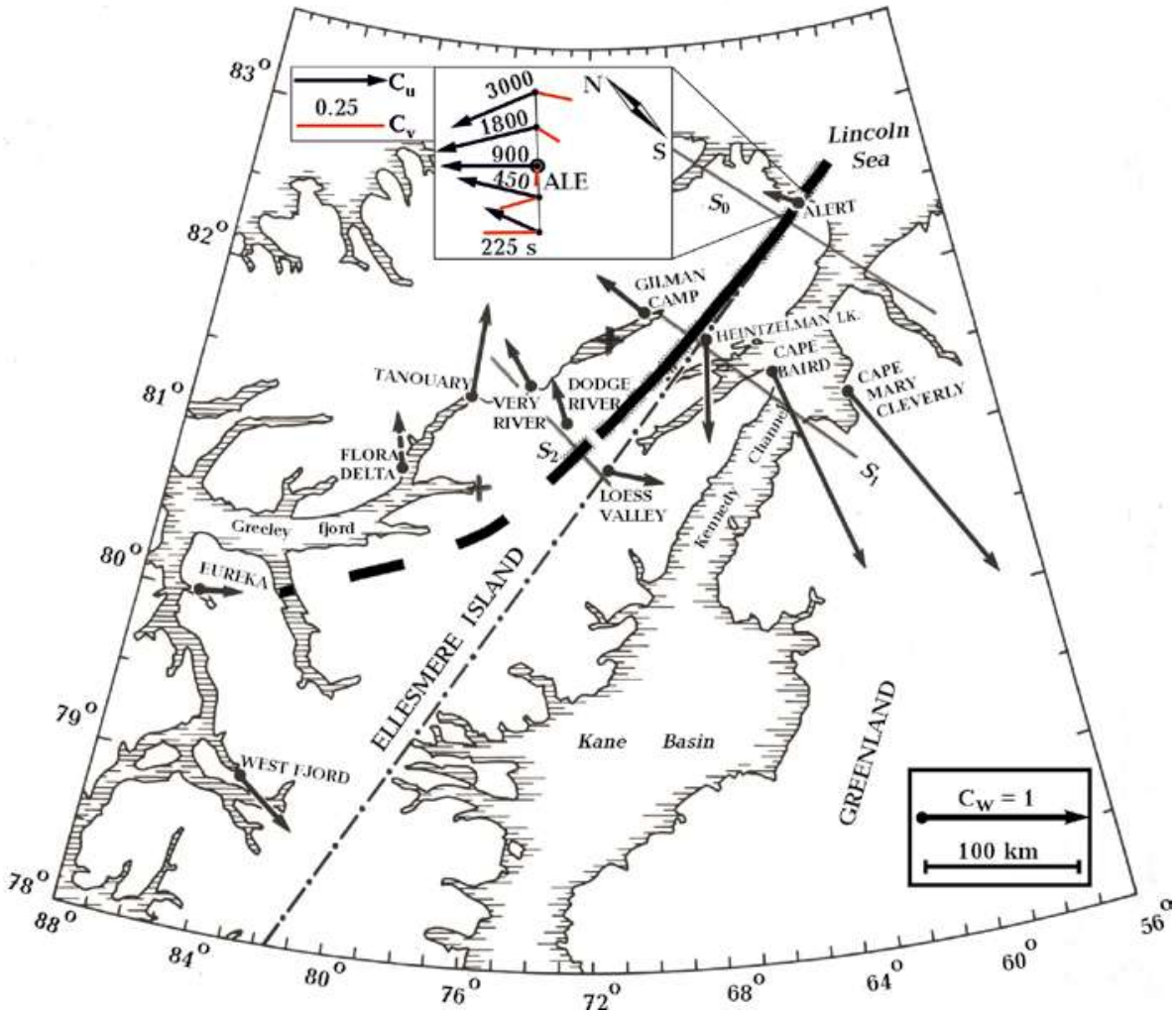

Fig. 11. ALE observatory (geomagnetic latitude φ_m=87.15°) and Alert conductivity anomaly (thick black line) drown by the data of Wiese induction arrows (≈$\mathbf{C}_u$) and horizontal anomalous field for periods 10—120 min [Praus et al., 1971; Rokityansky, 1975]. In the insert at upper part of the Figure, the results of our processing of the ALE modern observations are given.

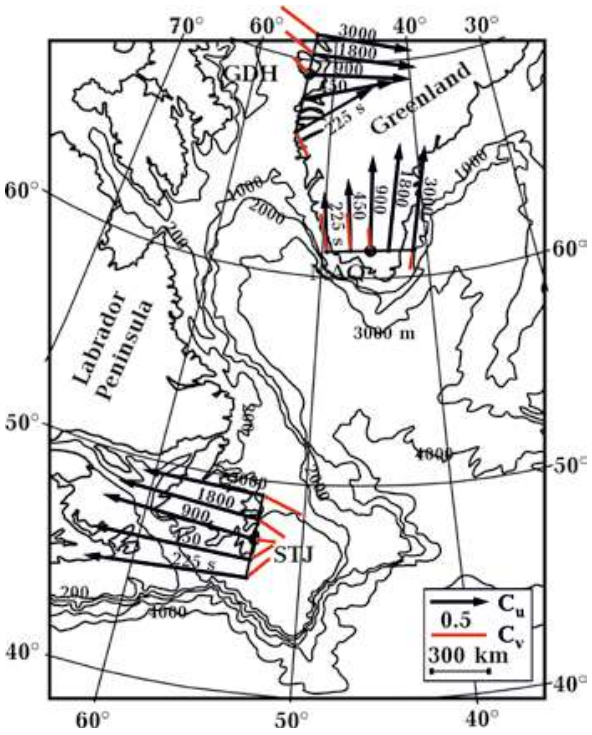

Fig. 12. Induction arrows at the observatories GDH, NAQ and STJ.

magnetic field showed that the SE component of the horizontal field is increased by a factor of 2—3 at the ALE observatory, at the Heintzelman and Loess Valley points, by 1.5—2 times at the Gilman Camp and Dodge River, and by a little less quantity at the Eureka. At the points of Cape Baird, Cape Mary Cleverly, Tanquary and West Fjord, the horizontal field is normal.

MTS curves were obtained in the range of 100—6000 s. Of the seven MTS curves presented in [Praus et al., 1971], five confidently showed the presence of a highly conductive body: under the ALE observatory at the depth h<4 km with longwise conductance approximately 7000 S, under the Heintzelman point — 18 km and 7000 S, under the Gilman Camp — 8 km and 9000 S, under the Loess Valley — 8 km and 18000 S, and under the Dodge River — 16 km and 8000 S. No crustal conductor was found on the MTS curves at points Cape Baird and Very River, where the anomaly in the horizontal components also was absent.

Of particular interest are the Wiese arrows at two points located southeast of the anomaly at a distance of 55 and 100 km from its axis, with magnitudes of 1.47 and 1.54, respectively. Between these points is Kennedy Channel, the anomalous field of which reduces the induction arrow at the nearest point (55 km) and increases it at the far one (100 km). Thus, in a wide stripe, including both banks of the Kennedy Channel, the induction arrow has a magnitude of 1.5±0.2; unfortunately, the frequency response was not determined, and the authors attributed the result to the wide interval of periods (10—120 min). It is interesting to note that the largest induction arrow of processed INTERMAGNET data (observatory STJ, see Fig. 12) has the same magnitude. Our modern processing of the modern digital INTERMAGNET data of the Alert Observatory (ALE) yields the induction arrows at five periods (see the insert in the upper part of Fig. 11). Their magnitude varies in ALE from 0.04 to 0.28 (for imaginary and real vectors). It is rather small, but quite robust. Indeed, the processing errors do not exceed 0.01 (see the ALE block in Fig. 7), but the anomalous fields recorded in ALE can be caused not only by currents in the studied quasi-2D Alert anomaly but also by any deflection from this model (for example deep channels in Lincoln Sea). However, let us try to interpret the vectors in ALE (see the insert at the upper part of Fig. 11). At the shortest period $\mathbf{C}_u$ and $\mathbf{C}_v$ are approximately parallel and of the same length. With an increase in the period, C_u increases to a maximum at T=1800 s, and C_v decreases to zero at T=900 s and tends to change sign. From these parameters, one can estimate T_0≈1500 s. This number is not proven explicitly (because of the rotation of vectors with a change in period) but the pattern of the frequency response obtained in ALE is in line with our quasi-2D theoretical expectations.

A high horizontal anomalous field in the NW-SE direction explains the abnormally high (above 0.6 for the periods 300—4000 s) input coherency between the northern and eastern components measured at ALE (see Fig. D1).

RES (φ_m=82.73°) north of Canada, the induction arrow is, on average, 0.2 directed to the north. At long periods (3000 and 1800 s), strong, nearly semi-annular variations are im-

posed on AV forming an irregular pattern. At short periods (450 and 225 s), AVs are small but clearly seen. The AV in RES is slightly smaller in amplitude than in THL but with a similar distribution over the components. Superposition of the variations with different periods changes sinusoidal form AV. For example, the lower extremum of the A_u and B_v components at observatories THL, RES, DRV, SBA is pointed, the upper one blunt, or in other cases, vice versa, the upper extremum is pointed, the lower one blunt (THL, SBA — on the B_u component).

TLH, ALE, **RES,** and **MBC** (φ_m=79.85°) are geomagnetically northernmost observatories. All four and only they in the northern hemisphere, having an intense diurnal variation of the geomagnetic field, do not contain its harmonics except very small second harmonic at some components (see Appendix, Fig. D). We checked antipode observatories in Antarctica and found that the spectra of three geomagnetic southernmost observatories **VOS** (φ_m=–88.36°), **DMC** (φ_m=–84.04°) and **SBA** (φ_m=–78.94°) are nearly similar to the spectra of the four northernmost observatories. We have not encountered in the literature the «bareness/nakedness» of the diurnal harmonic that we discovered at the highest geomagnetic latitudes. The described phenomenon is important for a more specific and correct description and modeling of the daily variations source in high latitudes.

GDH (φ_m=78.16°) is located on the southern cape of Disko Island near the western coast of Greenland (see Fig. 12). To the southwest of the observatory, a fiord with depths of more than 200 m bends next to it; to the west 100 km of shallow water, 100 km of a shelf 200—500 m deep and at a distance of ≈300 km the Baffin Basin (1.5—2 km deep) of the Baffin Sea. Sea currents yield an almost satisfactory explanation of the induction arrows in GDH. 150 km north of the observatory locates the crustal electrical conductivity anomaly Igdlorssuit [Wilhjelm, Friis-Christensen, 1974]. The anomalous field in the horizontal component attains a value of 2.5. In two field sites located to the west from anomaly axes, the induction arrows are directed to the west [Wilhjelm, Friis-Christensen, 1974], i.e., opposite to the coastal effect. It means that the crustal anomaly is of a larger scale than the coastal effect in Igdlorssuit. The southern continuation of the anomaly has not been explored. It may end before reaching the GDH, it may deviate to the West (but not to East) or pass directly under the GDH.

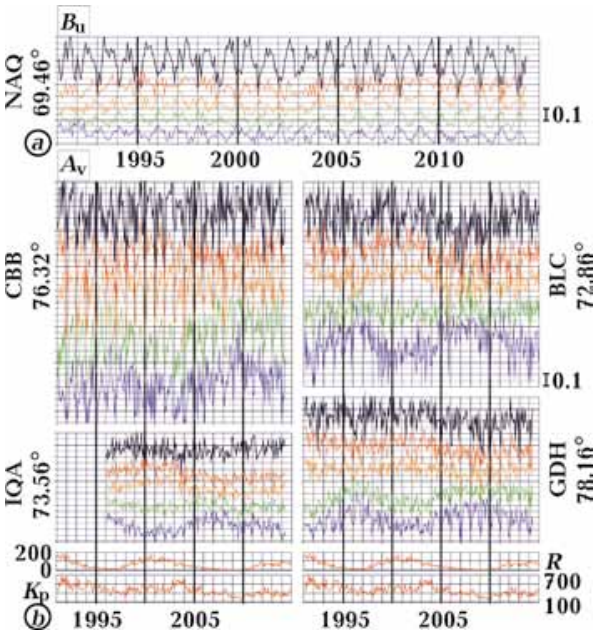

Fig. 13. Examples of the sign change of the induction arrow's periodic variations when the period changes. The curves are given in the following sequence of periods from top to bottom (3000, 1800, 900, 450, 225 s): *a* — reversal of the annual variation sign at the B_u component in NAQ, southern Greenland; *b* — sign reversal of the 11-year variation at the A_v component at four high-latitude North America observatories: CBB, IQA, BLC, and GDH. *R* is the index of solar activity (Wolf number), and K_p is the monthly sum of the planetary index of geomagnetic activity. All these graphs are given in colors in Appendix C.

It would be interesting to continue the study of the Igdlorssuit anomaly probably related to a rift-fault zone, and toclarify the possible moving of Greenland away from Baffin Island, supposed by some researchers [Wilhjelm, Friis-Christensen, 1974].

Temporal variations in GDH show fragments of 11-years SCV in several component-period units, especially interesting in the A_v component (see Fig. 13 and C1). SCV at three long periods and two short ones tend to have opposite signs. In two short periods, strong

SCV-2 (enhancement of AV with the 11-year envelope) was also observed. At A_u SCV has the same sign in all periods (see Fig. C1).

At the B_v component large AV were observed (up to 0.5 in the period 3000 s) in 1991—2003 years, but AV decreased by approximately twice after that. The opposite change, that is, an increase, was observed in THL on the A_u component (see Fig. C1).

NAQ (φ_m=69.46°) is located (see Fig. 12) near the southern extremity of Greenland in the aurora zone. Marine currents' concentration in the deep ocean surrounding the south of Greenland creates a significant real induction arrow in the northern direction, reaching the value of 0.8—1 at periods of 20—60 min. Consider in more details frequency characteristics of the NAQ Observatory presented in Fig. 12 for the components A_u and A_v at the periods 225, 450, 900, 1800, 3000 s: A_u=0.5, 0.6, 0.8, 0.92, 0.9; A_v=0.3, 0.3, 0.15, 0, –0.15. Maximum A_u and the sign change of A_v definitely yield the T_0=1800 s. According to the theory and empirical formula $G[\text{S}\times\text{m}]=5\cdot10^4\cdot\{T_0[\text{s}]\}^{1.2}$ [Rokityansky, 1982, p. 295, formula 6.63′ and Fig. 106] for the coastal effect with T=1800 s we obtain $G=5\cdot10^8$ S·m. The 2D regularities describe well the behavior of induction arrows in NAQ, even though the observatory is surrounded by the sea on three sides.

The B_u and B_v components are close to 0 on average, but the most intense AV are observed on the B_v component: at the longest periods, up to 0.5, decreasing at short periods to 0.25. For B_u, a change of the AV sign is observed with the period change: a positive AV up to 0.3 for the period 40—60 min and a negative value of about 0.1 at shorter periods (see Fig. 13). In NAQ, one of the largest in the world 11-year variations are observed in the A_u component with a magnitude of ≈0.1 at all periods (see Fig. 10). For the A_v and B_u components, the 11-year variations are also seen through a strong background of short-period variations. And quite unusual thing — a large trend of A_u component ≈0.2 over 23 years. This first exciting idea was to link this phenomenon to global warming. Indeed, the glaciers in Greenland are melting and since 1991, have retreated from its southern shores for tens of kilometers. It is quite likely that the anomalous trend of the induction arrow in NAQ is associated with the consequences of global warming. For example, it can be assumed that a little south of the observatory, practically non-conducting ice and/or frozen rocks were replaced by sea water, which brought sea currents closer to the observatory and increased the anomalous field at NAQ.

For **STJ** (φ_m=56.68°), the second (among 137 observatories) induction arrow $\mathbf{C}_u$ attains a value of ≈1.3, and this maximum is at short periods. $\mathbf{C}_v$ is directed opposite to $\mathbf{C}_u$, which means that the maximum $\mathbf{C}_u$ can be in an even shorter period. The deep sea surrounds STJ on three sides (see Fig. 12) and it is located at a distance of 400—500 km. Closer to STJ is located shallow the Great Newfoundland Bank with a sea depth of a few dozen meters. However, in a geological map under the Bank, the sediments up 5 km thick are shown. Their conductance is not shown but can be supposed to be ≈1000 S. Then currents of remote deep seas and the quasi-shelf of Newfoundl and Bank create local enhancement of induction arrow by means of cumulative effect. The same mechanism create the strongest induction arrow in the DRV observatory. The environmental setting of the sea depths is rather complex around STJ but the 2D approach yields a satisfactory description of the observed data.

HLP (φ_m=53.06°) is an ordinary mid-latitude observatory in Poland with well-pronounced pure sinusoidal AV at meridional components at long periods. In 2008, intense quasi-annual variations and a strong trend appeared at short periods. In [Babak et al., 2017], possible geodynamic reasons for the trend were considered in detail, but no conclusions were drawn. It is desirable to check each trend by extending observations until today. The trend in HLP might be related to DC railway noise interference.

KOU (φ_m=14.57°) is a low-latitude near-equatorial observatory in Guyana near the Atlantic Ocean with a coastal effect, which caused the real induction arrow of 0.8—0.9 and an imaginary one close to 0. At the two shortest periods in 1996—1999, anomalous

variations were observed, probably caused by noise; after 2008 and until 2014, intense (0.15) for middle and low latitudes AV occurred in the eastern B_u component synchronously with no less intense quasi-annual variations in the HLP. Remote connection? Unlikely. Although in these years, the intensification/appearance of annual variations was also observed at several observatories, particularly in Japan, and there we qualify them as a possible medium-term precursor of the Tohoku earthquake [Rokityansky et al., 2019a,b]. The 11-year variation with an amplitude up to 0.15 at the longest period was observed at some components, which provides ground to assume that low latitudes, along with high latitudes [Babak et al., 2017]), are favorable zones for the appearance of 11-year variations.

HER (φ_m=–33.91°) is in South Africa on the Atlantic side of the Cape Good Hope 100 km to SE from the city of Cape Town. Deep water isolines run along the coast in NNW-SSE direction at the distance ≈150 km from coast. The normal to deep sea currents are directed to ENE, but induction arrows are directed to NNE. The reason for this is that 400 km to the SSE the deep water isolines turn 90 degrees to the left and deep-sea currents flow in the direction of ENE. Being 2.5 times farther away from the observatory than the currents along the coast, they only slightly deflect the induction arrows to the NW, and most strongly deflect the longest period, which decays more slowly during propagation. The induction arrow attains maximal value of 1 at the period of 3000 s.

DRV (φ_m=–74.11°) and **SBA** (φ_m=–78.94°) are Antarctic observatories characterized by high-latitude behavior. AV there is the larger, the longer the period. At DRV, the AV amplitude is comparable to the maximum amplitudes of high-latitude observatories in the northern hemisphere. At the SBA, the AV amplitudes are approximately one and half times smaller, and the A_u polarity is positive, i.e., its sign differs from the normal one for high latitudes. In DRV the induction arrow is the largest (1.5) among INTERMAGNET observatories.

Discussion. ***Periodic variations***. *Periodic Annual variations of the induction arrow, global data*. Annual variations are clearly observed at 2/3 of observatories. However, they exist anytime and anywhere because the magnetosphere-ionosphere source of the geomagnetic field varies during the year, which creates a source effect. This effect depends in a complex way on the regional and local properties of the source, on the geoelectric structure, on the magnitude and parameters of extraneous fields (noise) at the observatory. AVs with significant amplitude can become an interference when studying the electrical conductivity of the Earth. Fig. 9 shows variations of the induction arrow at 25 observatories, representing all latitudes from north to south, where clear annual variations are visible on at least one of the four components. Fig. 10 and Appendix C present variations for North America region. We can see that at high geomagnetic latitudes >65°, AV attains a range/(double) amplitude of up to 0.4—0.5 for some components, periods, observatories. At the middle and low latitudes, the range decreases to 0.05—0.015.

Another AV characteristic important for the identification of its physical nature is the AV sign. In [Araya, Ritter, 2016] and earlier studies, no more than 12 observatories and only mid-latitude ones were studied, and it was concluded that the northern component A_u of the annual variation is always positive (it has a maximum in June and a minimum in December). Our global study confirmed these earlier results in the low and middle latitudes but in almost all high-latitude observatories, the A_u polarity is negative (see Figs. 6, 9, 10, Appendix C). Therefore, the model of the source of annual variations developed in [Araya, Ritter 2016] does not explain the phenomenon on a global scale. Our global results show that the AV source is not located at high magnetosphere altitudes (ring currents) but in the ionosphere of the aurora zone and its mid- and high-latitude spreading currents. It is an important result.

The sign of periodic variations can change when the period changes (see Fig. 13, *a*).

11-years or Solar Cycle Variation (SCV). The 11-year variation is less studied: half of

the observatories do not have a long enough record to distinguish it. In the remaining half, this variation is visible at 1/3 of the observatories, mostly in North America and Europe, equatorial Africa and America, and on the southern islands of the Indian Ocean. An amplitude of less than 0.05 is difficult to recognize, especially against the background of intense variations of a shorter period. The observed SCV amplitudes vary from 0.05 to 0.3. Cases have been observed several times where opposite SCV signs were seen on the same component at different periods (Fig. 13, *b*).

Induction arrow daily variations, one case. This study was made with the synchronous 1-sec records of two middle-latitudinal east-European observatories, KIV and SUR, 640 km apart. The records from each observatory were processed independently using the Klymkovych program. Daily changes in the real induction arrow are shown in Fig. 14, which shows that in the evening and at night, the induction arrows are concentrated in a compact, almost isometric area. In the mor-

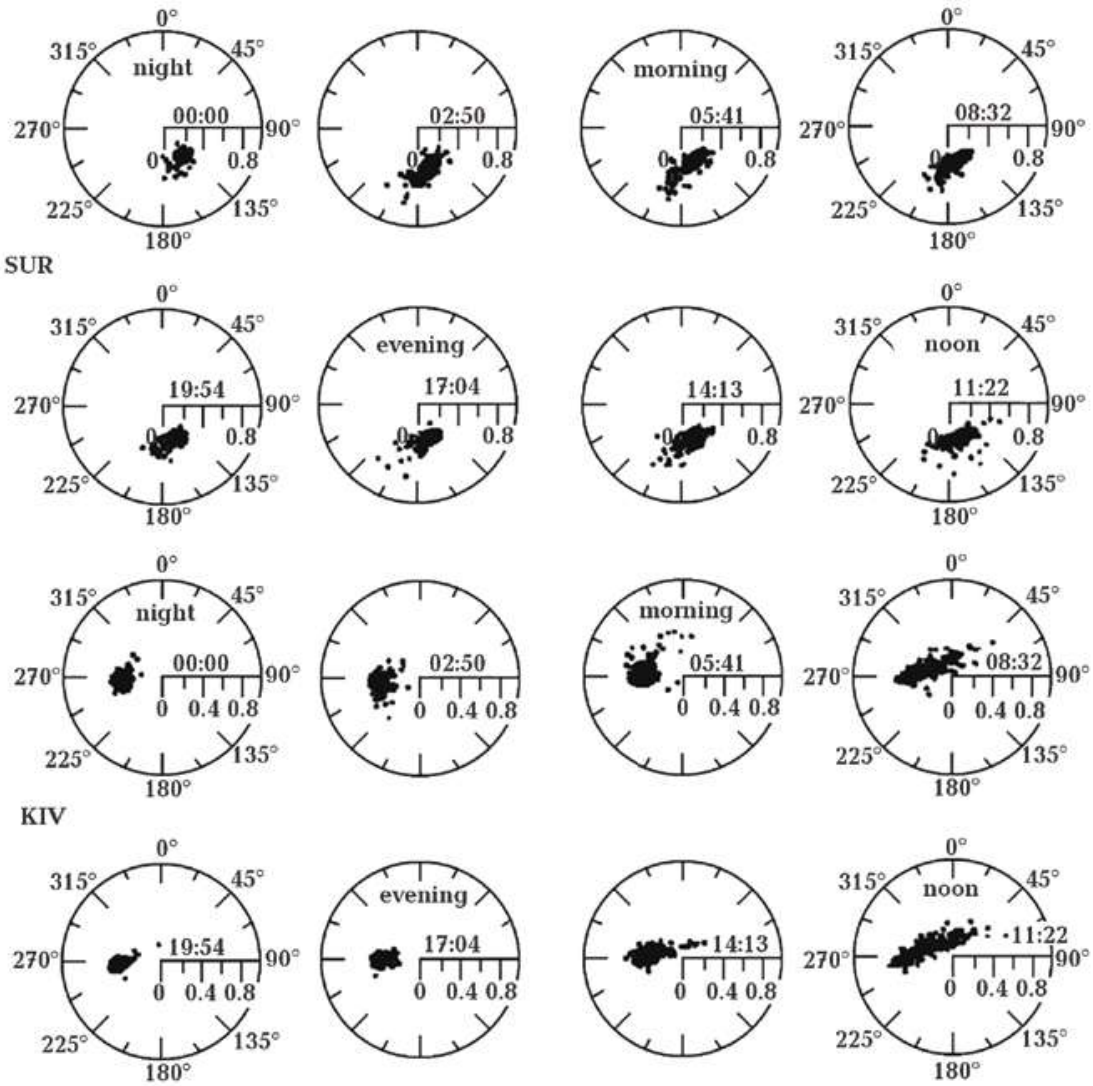

Fig. 14. Polar diagrams of the real induction arrows $\mathbf{C}_u$ of the SUR and KIV observatories for a 5—10 min period, built for eight successive intervals of a day with a duration of 10260 s=2 h 51 min. The induction arrow starts at the center of each circle, and its arrow (tip) every day draws a point. There are 366 points inside each circle — the number of days in 2008. The radius of each circle=1. The numbers below the horizontal semi-axis mark the 0.4 and 0.8 parts of this unit. The numbers above the horizontal semi-axes indicate the local start time of the recording used for the processing. The pre-midnight interval of 1 hour and 15 minutes was not used.

ning and afternoon hours, this area expands, the center of the point cloud shifts, and a daily variation of the induction arrow appears. All this can be explained as follows: nighttime variations at mid-latitude observatories (bays and Pi pulsations) are mainly the fields of spreading currents of a polar electrojet, that is, a remote and, therefore, a rather homogeneous source. The T-C model is mostly fulfilled, the induction arrow occupies a compact area, and individual surges are caused by magnetic storms or random noise. The sources of daytime variations (Pc3, Pc4, Pc5 pulsations, etc.) are resonances of various types of hydromagnetic waves propagating in magnetospheric cavities based upon an unstable, well-conducting daytime ionosphere. The T-C model is fulfilled to a lesser extent, the estimates of the RF are scattered and shifted, and a daily variation of the induction arrow appears. With this rather obvious physical explanation, it can be assumed that diurnal variations are common and widespread. Approximately the same difference exists for the summer and winter variations, consequently the above explanation can be also valid for the annual variation. If annual variations are presented in the form of the circle diagrams, as in Fig. 14, we can compare diurnal and annual variations shown identically as the circle diagrams, we clearly see similar behavior during winter — night and summer — day.

Harmonics of the diurnal period in geomagnetic field spectra and coherences. Having calculated coherences up to 10^5 s, we noticed extrema at the diurnal period 86400 s and its harmonics. To better understand this result, we calculated spectra for all North America stations.

The spectra of geomagnetic field components were calculated by Fourier transform of the 1-year-long (mainly 2001) magnetic field time series, and spectra from 10 min up to 1 month were obtained for all observatories show in Fig. D1. All spectra follow the well-known pattern: the amplitude of the geomagnetic field grows with an increase in period. However, in the vicinity of the diurnal period, a more or less flat maximum is usually observed, and at exactly the diurnal period, an intense line is always presented. In the observatories closest to the geomagnetic pole, it is a single line (without harmonics). At mid- and low-latitude observatories, the diurnal line is accompanied by a set of lines corresponding to the second, third, fourth, and sometimes fifth-seventh harmonics (TUC, FRN, DLR, etc.). The amplitude ratio of these lines varies from one station to another and also from one component to another at the same observatory. Such a diversity is evidences of the complex formation of diurnal variations and the involvement of external (related to source) and internal (related to conductivity distribution) factors in this process. Consider the most interesting features of the observatory data presented in Fig. D1.

In ALE (geomagnetic latitude 87.15°) spectra we see strong diurnal lines at all components and a small semi-diurnal line at *X*-component. In Coh2IN and Coh2Multy we see only one line — the diurnal. About the same spectra are in TLH (87.31°), RES (82.73°) and MBC (79.85°) — all the observatories are inside the polar cap not far from the geomagnetic pole. Horizontal components' amplitude is much bigger than vertical one.

The next 11 observatories are located in the aurora zone or near its border. Consider some observatories from this zone with typical behavior:

– in GDH (78.16°) at *X*-component the second harmonics predominates, at *Y*- and *Z*-component the first harmonic dominates. In Coh2IN and Coh2Multy the first and second harmonics are equally presented;

– in BLC (72.86°) and IQA (73.55°) at *X* the first and second harmonics are of equal value, at *Y* and *Z* the first harmonic predominates. In coherences only the first harmonic well presented, second one — presented weaker.

The next 10 observatories are located in the middle latitudes 40—62°:

– in SIT, not far from the aurora zone, in *X* we see two harmonics, in *Y* — three, in *Z* — one harmonic;

– in VIC, 1240 km to the south, in *X* — there are three harmonics, in *Y* — four, in *Z* — two harmonics.

Some conformity between spectra and co-

herencies is observed but not very straightforward. Father to south, the conformity improves.

The middle latitude observatories BSL (39.65°), TUC (39.56°), DLR (37.96°), TEO (28.5°), SJG (27.92°) and HON (21.58°) we relate to low latitudes where the main part of S_q ionospheric current system located. Almost all middle and low latitude observatories have the «right» interrelation of harmonics: the first harmonic dominates; every higher-order harmonic has a lesser amplitude compared with a lower-order one.

There is one small exception to the last rule: at BSL, TUC and DLR the second harmonic a little larger than the first one at *X*-component only. All three observatories are located at nearly the same latitude and this effect seemingly appears to be related to the position of S_q current system.

It should also be noted that observatories SBL, TEO and CRP have lowered Coh2Multy at short periods T<500 s. Such behavior is typical for strong noise in these periods, for example from DC railways [Aleksanova et al., 2003].

In HON at *X* we see four harmonics, at *Y* — six harmonics, and at *Z* — seven harmonics. The same regularity we see in coherences: Coh2IN has four harmonics and Coh2Multy has all seven harmonics with monotonically decreasing amplitudes — a classical case.

Figs. B1—B3 presents the great magnetic storm variation and quiet solar-day variation at different latitudes which can help visualize the formation of spectral lines.

A periodic variations and trends. A lot can be written on this topic: changes in the induction arrow during geodynamic processes, which can be caused by two very different phenomena: the change of the electrical conductivity in the solid-liquid earth or the radiation of lithospheric emission field with its own B_z/B_{xy} ratio, or by trivial noise e.g. from DC railway. We will briefly consider only the trends that appear in our 23-year long records.

The most interesting trend was obtained at the NAQ Observatory in south Greenland: A_u component increased by 0.2 in 23 years (see Fig. 10, C1) [Babak et al., 2017]. At the same time, there was a particularly intense melting of glaciers which retreated from Greenland's southern shores for tens of kilometers. It is quite likely that the anomalous trend of the induction arrow in NAQ is associated with the consequences of global warming.

At the HLP observatory (Poland) a trend of ≈0.3 was recorded only at periods <10 min during the years 2008—2014. The article of [Babak et al., 2017] discusses this event. Most likely, this trend is a result of the currents from the DC railway.

In some observatories within the auroral zone, trends of order 0.1 are observed. They can be related with an extraordinary large moving of the Northern Magnetic (not the Geomagnetic) Pole — 1100 km in 23 years.

Magnitude of induction arrows for studied periods 150—6000 s. As can be seen in Fig. 8 and other presented materials the majority of the induction arrows have magnitudes ranging from 0.2 to 0.6. The higher values are found at a few coastal observatories and some crustal anomalies. In the INTERMAGNET network, the maximum tipper magnitude was observed at coast al observatories DRV, Antarctica 1.5 and STJ, Newfoundland 1.3, and those maxima observed at the shortest periods inherent to shelf depth. The maximum tipper for inland anomalies are on the Donbas anomaly, Ukrainian site PYAT in Fig. 4 [Rokityansky et al., 1989] with magnitude of 1.6 and on the Alert anomaly, Canada site Cape Mary Cleverly in Fig. 11 [Praus et al., 1971] with magnitude of 1.5.

Conclusions. 137 globally distributed INTERMAGNET observatories were processed, and temporal variations of the induction arrow were obtained for the first time in the high geomagnetic latitudes, which allows us to draw the following new conclusions:

– annual variation of the induction arrow at high geomagnetic latitudes over 65° has a range (double amplitude) of up to 0.4—0.5 for some components, periods, observatories and, as a rule, a negative sign at A_u (maximum in December, minimum in June in both hemispheres). At middle and low latitudes, the range decreases to 0.05—0.015, and the sign of the northern A_u component is positive.

The annual variation is visible in about 2/3 of the records;

– the obtained data on AV signs showed the invalidity of the previous theory suggesting the AV source at the altitude of the ring currents. The sharp sign change in the aurora zone border shows that the AV source is in the ionosphere;

– 11-year or Solar Cycle Variations (SCV) were identified in 1/3 of observatories. Their amplitude span from 0.05 (threshold from the shorter periods background) to 0.3. Several cases of SCV polarity changes were observed at the period change;

– a significant trend of magnitude 0.2 for all periods was observed in southern Greenland, coinciding with the rapid glacier melt over the past 30 years, suggesting a possible connection between this trend and global warming. In some observatories in the aurora zone, trends of order 0.1 were observed. They can be related with extraordinary large moving of the Northern Magnetic (not Geomagnetic) Pole — 1100 km in 23 years;

– at geomagnetic latitudes φ_m from –78° to +78°, the main harmonic (24 hours=86400 s) of daily variations of the geomagnetic field is always accompanied by at least one higher-order harmonic 24/*n* (*n*=1÷7). At higher latitudes $|\varphi_m|>78°$ of both hemispheres only the fundamental 24-hour harmonic is visible, bare of higher order harmonics, and here, the vertical component of the geomagnetic field is much smaller than the horizontal one. This is an important result for the constructing a geomagnetic field source in circumpolar zones;

– the magnitude of the induction arrow variations is not(in the first approximation) related to the magnitude and direction of the arrow itself.

Acknowledgements. The authors express their gratitude to Iv.M. Varentsov and T.A. Klimkovich for providing the data processing programs, to V.I. Babak for processing a significant amount of data, to INTERMAGNET for making available the observatories' data, and to the staff of geomagnetic observatories for the high-quality measurements.

Data availability. Most of the geomagnetic data for this article are available at INTERMAGNET sitehttps://www.intermagnet.org/. The rest of the data are available at the World Data Center for Geomagnetism (Kyoto) site https://wdc.kugi.kyoto-u.ac.jp/wdc/Sec3.html.

References

Aleksanova, E.D., Kulikov, V.A., Pushkarev, P.Yu., & Yakovlev, A.G. (2003). The use of fields of electrified railways when conducting electromagnetic soundings. *Izvestiya vuzov. Geology and exploration,* (4), 60—64 (in Russian).

Araya, J.V., & Ritter, O. (2016). Source effects in mid-latitude geomagnetic transfer functions, *Geophysical Journal International, 204*, 606—630.https://doi.org/10.1093/gji/ggv474.

Babak, V.I., Rokityansky, I.I., Sokolova, E.Yu., & Tereshyn, A.V. (2017). Annual, 11-year and aperiodic variations of the induction vector at 8 observatories of the Intermagnet network, *Geofizicheskiy Zhurnal, 39*(1), 97—110. https://doi.org/10.24028/gzh.0203-3100.v39i1.2017.94013 (in Russian).

Klymkovych, T.A. (2009). Peculiarities of temporal changes of anomalous magnetic field and induction vectors in Transcarpathian seismically deflected deflection. *Candidate's thesis*. Kyiv (in Ukrainian).

Kuvshinov, A., Grayver, A., Töfner-Clausen, L., & Olsen, N. (2021). Probing 3-D electrical conductivity of the mantle using 6 years of Swarm, CryoSat-2 and observatory magnetic data and exploiting matrix Q-responses approach. *Earth, Planets and Space, 73*(67). https://doi.org/10.1186/s40623-020-01341-9.

Law, L.K., Laurier, I.M., Andersen, F., & Whitham, K. (1963). Investigations during 1962 of the Alert anomaly in geomagnetic variations. *Canadian Journal of Physics, 41*, 1868—1882. https://doi.org/10.1139/p63-187.

Praus, O., Laurier, I.M., & Law, L.K. (1971). The extension of the Alert geomagnetic anomaly through northern Ellesmere Island Canada. *Canadian Journal of Earth Sciences, 8*(1), 50—64. https://doi.org/10.1139/e71-003.

Rigaud, R., Kruglyakov, M., Kuvshinov, A., Pinheiro, K., Petereit, J., Matzka, J., & Marshalko, E. (2021). Exploring effects in tippers at island geomagnetic observatories due to realistic depth- and time-varying oceanic electrical conductivity. *Earth Planets Space, 73*(3). https://doi.org/10.1186/s40623-020-01339-3.

Rokityansky, I.I. (1982). *Geoelectromagnetic investigation of the Earth's crust and upper mantle*. Berlin-Heidelberg-New York: Springer Verlag, 381 p.

Rokityansky, I.I. (1975). *Investigation of electrical conductivity anomalies by magnetovariational profiling method*. Kiev: Naukova Dumka, 280 p. (in Russian).

Rokityansky, I.I., Ingerov, A.I., Baysarovich, M.N., Dzyuba, K.I., Zamaletdinov, A.A., Lysenko, E.S., Popov, V.M., Rokityanskaya, D.A., & Shuman, V.N. (1989). Donbass electrical conductivity anomaly. *Geofizicheskiy Zhurnal, 11*(3), 30—40 (in Russian).

Rokityansky, I.I., Babak, V.I., & Tereshyn, A.V. (2019a). Low-Frequency Electromagnetic Signals Observed before Strong Earthquakes. In *Seismic Waves: Probing Earth System* (pp. 89—106). IntechOpen. https://doi.org/10.5772/intechopen.88522.

Rokityansky, I.I., Babak, V.I., Tereshyn, A.V., & Hayakawa, M. (2019b). Variations of Geomagnetic Response Functions before the 2011 Tohoku Earthquake. *Open Journal of Earthquake Research, 8*, 70—84. https://doi.org/10.4236/ojer.2019.82005.

Schmucker, U. (1964). Anomalies of geomagnetic variations in the southwestern United States. *Journal of Geomagnetism and Geoelectricity, 15*(4), 193—221. https://doi.org/10.5636/jgg.15.193.

Schmucker, U. (1970). *Anomalies of geomagnetic variations in the southwestern United States*. University of California Press, 165 p.

Varentsov, I.M. (2007). Arrays of Simultaneous Electromagnetic Soundings: Design, Data Processing and Analysis. In V.V. Spichak (Ed.), *Electromagnetic Sounding of the Earth's Interior: Theory, Modeling, Practice* (pp. 263—277). Amsterdam: Elsevier.

Varentsov, I.M., Sokolova, E.Yu., Martanus, E.R., & Nalivaiko, K.V. (2003). Technique for constructing EM field transfer operators for the array of synchronous soundings BEAR. *Fizika Zemli,* (2), 30—50 (in Russian).

Wilhjelm, J., & Friis-Christensen, E. (1974). The Igdlorssuit geomagnetic variation anomaly in the rift-fault zone of northern west Greenland. *Journal of Geomagnetism and Geoelectricity, 26*(9), 173—189. https://doi.org/10.5636/jgg.26.173.

Просторово-часові варіації індукційної стрілки

І.І. Рокитянський, А.В. Терешин, 2024

Інститут геофізики ім. С.І. Субботіна НАН України,
Київ, Україна

Вектор індукції **C** — є характеристикою змінного геомагнітного поля в одній точці спостереження (x, y) для певного періоду T геомагнітних варіацій **B**. Він наочно описує величину та напрямок відхилення вектора геомагнітного поля від горизонтальної площини. Вектор індукції не є нульовим лише тоді, коли з'являється вертикальна компонента B_z. Вона з'являється у таких випадках: 1) за наявності горизонтальних градієнтів електропровідності під поверхнею Землі; 2) в разі неповної компенсації вертикальної компоненти первинного поля іоносферно-магнітосферного джерела вторинним полем, індукованим у горизонтально-шаруватій Землі; ступінь компенсації систематично змінюється протягом дня, року …, що зумовлює тимчасові коливання вектора індукції (ефект джерела); 3) поява невидаленого шуму або емісії літосфери, що містить B_z. Розглянуто просторову та часову мінливість вектора індукції. Реальні (у фазі) та уявні (позафазно) вектори індукції (вертикальна функція

відгуку, або типер) отримані для кожної доби під час відповідних спостережень з 1991 по 2014 р. для п'яти інтервалів періодів, с: 150—300, 300—600, 600—1200, 1200—2400, 2400—3600, що розраховані за трьома компонентами геомагнітного поля, зареєстрованими на 137 обсерваторіях глобальної мережі INTERMAGNET. Щоб зменшити розкид, щоденні значення було перераховано у місячні значення. Такий глобальний матеріал від +87° до –88° геомагнітної широти отримано вперше, його аналіз дає нові наукові результати. Річні варіації (із періодом 1 рік) спостерігаються приблизно на 2/3 обсерваторій (у решті обсерваторій вони нижчі за фоновий рівень варіацій коротких періодів і/або шуму). Його амплітуда сильно залежить від геомагнітної широти та іноді досягає такого високого значення — 0,4—0,5 (від піку до піку) у високих (>65°) широтах і змінюється у межах 0,01—0,15 у середніх і низьких широтах. Попередні дослідження у середніх широтах виявили, що річна варіація північної компоненти A_u є скрізь додатною (максимум — у червні, мінімум — у грудні), тому для пояснення річних варіацій було запропоновано модель глобального джерела у вигляді кільцевого струму на висоті 3—6 радіусів Землі. Ми виявили, що у високих широтах A_u зазвичай є від'ємною, і пропонуємо пояснити всі спостережувані особливості річних варіацій вектора індукції варіаціями іоносферних струмів у зоні полярних сяйв. 11-річні варіації трапляються у ≈30 % обсерваторій, розташованих на всіх широтах, але частіше у зонах полярних сяйв. У кількох обсерваторіях було виявлено монотонні зміни векторів — тренди. Найбільший тренд величиною 0,2 для всіх періодів був виявлений на півдні Гренландії, де льодовики швидко тануть за останні 30 років, що дає можливість пов'язати обидва тренди із глобальним потеплінням. У декількох авроральних обсерваторіях Північної Америки було помічено тренди величиною ≈0,1. У ці самі роки Північний магнітний полюс надзвичайно швидко перемістився на 1100 км за 23 роки. Можна припустити, що ці тенденції пов'язані зі зміною позиції аврорального овалу. На геомагнітних широтах від –78° до +78° основна гармоніка (24 год=86400 с) добових варіацій геомагнітного поля завжди супроводжується принаймні однією гармонікою вищого порядку 24/n (n=1÷7). На вищих широтах >78° обох півкуль існує лише основна 24-годинна гармоника. Часові варіації вектора індукції можуть створювати труднощі у визначенні їх постійної складової, яка використовується для вивчення електропровідності земної кори та верхньої мантії, але можуть бути корисними для вивчення геодинамічних процесів.

Ключові слова: електричні властивості, електромагнітна теорія, геомагнітна індукція, магнетотелурика, аналіз часових варіацій.

Appendix A. Observatories processed in this study

Table A1. INTERMAGNET observatories processed in this study, geomagnetic coordinates are given for the year 2010

Code	Station	Geom. lat.	Geom. long.	Geogr. lat.	Geogr. long.	Processed years
THL	Qaanaaq (Thule)	87.31	14.00	77.468	–69.227	1991—2014
ALE	Alert	87.15	153.09	82.497	–62.353	1992, 1995—1997, 2002, 2010—2011
RES	Resolute Bay	82.73	–54.06	74.69	–94.895	1992—2014
MBC	Mould Bay	79.93	–92.93	76.315	–119.362	1991—1997
GDH	Godhavn	78.16	33.80	69.251	–53.533	1991—2014
CBB	Cambridge Bay	76.32	–55.24	69.123	–105.031	1991—2014
HRN	Hornsund	73.91	125.30	77	15.55	2002—2014
IQA	Iqaluit	73.55	5.80	63.753	–68.518	1996—2014
BLC	Baker Lake	72.86	–36.62	64.318	–96.012	1991—2014

Code	Station	Geom. lat.	Geom. long.	Geogr. lat.	Geogr. long.	Processed years
BRW	Barrow	69.68	–112.56	71.32	–156.62	1991—2014
NAQ	Narsarsuaq	69.46	38.50	61.167	–45.433	1991—2014
YKC	Yellowknife	68.71	–59.38	62.483	–114.482	1992—2014
FCC	Fort Churchill	67.57	–30.60	58.759	–94.088	1991—2014
ABK	Abisko	65.98	114.32	68.358	18.823	1994—2014
CMO	College	65.36	–97.24	64.871	–147.86	1991—2014
PBQ	Poste-de-la-Baleine	65.02	–7.51	55.277	–77.745	1992—2007
SOD	Sodankyla	63.87	119.74	67.37	26.63	1991—2014
LYC	Lycksele	62.55	110.78	64.612	18.748	2008—2014
LER	Lerwick	61.75	88.77	60.138	–1.183	1991—2014
MEA	Meanook	61.29	–52.80	54.616	–113.347	1991—2014
SIT	Sitka	60.19	–78.62	57.06	–135.33	1991—2014
UPS	Uppsala	58.35	106.15	59.903	17.353	2003—2014
GLN	Glenlea	58.28	–31.38	49.645	–97.12	1992—1997, 2002—2006
LOV	Lovoe	57.74	106.23	59.34	17.82	1991—2004
NUR	Nurmijarvi	57.74	113.04	60.51	24.66	1991—2014
ESK	Eskdalemuir	57.53	83.65	55.32	–3.206	1991—2014
STJ	St John's	56.68	24.33	47.595	–52.677	1991—2014
VAL	Valentia	55.47	74.60	51.933	–10.25	2002—2014
BFE	Brorfelde	55.25	98.40	55.625	11.672	1991—2013
OTT	Ottawa	55.18	–4.12	45.403	–75.552	1991—2014
NEW	Newport	54.57	–54.46	48.271	–117.12	1991—2014
SHU	Shumagin	54.24	–102.36	55.35	–160.46	2005—2014
WNG	Wingst	53.88	94.92	53.725	9.053	1994—2014
VIC	Victoria	53.89	–61.56	48.52	–123.42	1991—2014
HAD	Hartland	53.60	80.16	51	–4.48	1991—2014
BOX	Borok	53.33	123.50	58.07	38.23	2004—2014
HLP	Hel	53.06	104.57	54.6035	18.811	1998—2014
YAK	Yakutsk	52.37	–163.24	61.96	129.66	2011—2014
ARS	Arti	49.12	140.01	56.433	58.567	2011—2014
MGD	Magadan	52.02	–146.26	60.051	150.728	2010—2014
NGK	Niemegk	51.66	97.62	52.07	12.68	1995—2014
MAB	Manhay	51.17	90.05	50.298	5.682	2005—2014
DOU	Dourbes	51.16	88.90	50.1	4.6	2002—2014
BEL	Belsk	50.06	105.17	51.836	20.789	1993—2014
CLF	Chambon la Foret	49.57	85.71	48.025	2.26	1991—2014
BFO	Black Forest	48.81	91.83	48.331	8.325	2006—2013
BDV	Budkov	48.55	97.64	49.08	14.02	1994—2014
FUR	Furstenfeldbruck	48.14	94.65	48.17	11.28	1995—2014
BOU	Boulder	48.06	–38.69	40.14	–105.233	1991—2014
FRD	Fredericksburg	47.96	–6.07	38.21	–77.367	1991—2014
LVV	Lviv	47.70	107.14	49.9	23.75	2004—2014
KIV	Kiev	47.43	113.47	50.72	30.3	2009—2014

Code	Station	Geom. lat.	Geom. long.	Geogr. lat.	Geogr. long.	Processed years
NCK	Nagycenk	46.69	99.67	47.63	16.72	1993, 1995—2014
HRB	Hurbanovo	46.67	101.16	47.873	18.19	1997—2014
PET	Paratunka	45.86	–137.96	52.971	158.248	2011—2015
THY	Tihany	45.78	100.52	46.9	17.89	1991—2014
NVS	Novosibirsk	45.42	159.97	54.85	83.23	2003—2014
FRN	Fresno	43.24	–54.04	37.091	–119.72	1991—2014
EBR	Ebro	43.04	81.30	40.957	0.333	2002—2014
GCK	Grocka	43.09	102.49	44.633	20.767	2005—2014
SPT	San Pablo-Toledo	42.46	76.12	39.55	–4,35	1997—2014
SUA	Surlari	42.22	107.68	44.68	26.25	1999—2014
AQU	L'Aquila	42.18	94.61	42.38	13.32	2000—2013
IRT	Irkutsk	42.11	177.23	52.27	104.45	1998—2014
DUR	Duronia	41.05	95.24	41.39	14.28	2012—2013
PAG	Panagjurishte	40.46	105.06	42.515	24.177	2007—2014
SFS	San Fernando	39.92	73.67	36.667	–5.945	2005—2014
BSL	Stennis Space Center	39.65	–19.65	30.35	–89.64	1991—2014
TUC	Tucson	39.57	–43.24	32.174	–110.73	1991—2014
KHB	Khabarovsk	38.36	–157.02	47.61	134.69	2012—2014
ISK	Kandilli	38.23	109.25	41.063	29.062	2001—2009
DLR	Del Rio	37.95	–32.08	29.49	–100.917	1991—2010
IZN	Iznik	37.58	109.72	40.5	29.72	2007—2014
PEG	Pedeli	36.2	103.56	38.1	23.9	2010—2014
MMB	Memambetsu	35.44	–148.24	43.91	144.19	1993—2012
AAA	Alma Ata	34.31	153.01	43.25	76.921	2005—2014
CNH	Changchun	34.29	–165.16	44.08	124.86	2011—2014
WMQ	Urumgi	34.16	162.52	43.81	87.71	2011—2014
GUI	Guimar-Tenerife	33.42	60.85	28.321	–16.441	1997—2014
BMT	Beijing Ming Tombs	30.22	–172.56	40.3	116.2	1998—2014
QSB	Qsaybeh	30.14	113.69	33.871	35.644	2000—2009
TEO	Teoloyucan	28.45	–29.07	19.747	–99.182	2002—2011
SJG	San Juan	27.92	6.53	18.111	–66.15	1991—2014
KAK	Kakioka	27.47	–150.78	36.232	140.186	1956—2015
CYG	Cheongyang	26.69	–162.84	36.37	126.854	2013—2014
LZH	Lanzhou	25.94	176.45	36.087	103.845	2001—2014
MID	Midway Island	25.03	–109.94	28.21	–177.38	2000—2005
TAM	Tamanrasset	24.41	82.03	22.79	5.53	1993—2014
KNY	Kanoya	22.00	–158.80	31.42	130.88	1991—2016
HON	Honolulu	21.58	–89.71	21.32	202	1991—2014
MBO	Mbour	19.82	57.81	14.392	–16.96	1993—2014
JAI	Jaipur	18.19	150.14	26.92	75.8	2011—2014
LNP	Lunping	15.12	–167.44	25	121.167	1995, 1997—2000
KOU	Kourou	14.57	20.07	5.21	–52.73	1996—2014
GZH	Zhaoging	13.88	–175.61	23.97	112.45	2003—2014

Code	Station	Geom. lat.	Geom. long.	Geogr. lat.	Geogr. long.	Processed years
PHU	Phuthuy	10.92	178.26	21.029	105.96	1996—2014
ABG	Alibag	10.26	146.53	18.638	72.872	1997—2014
HYB	Hyderabad	8.55	151.86	17.42	78.55	2009—2014
AAE	Addis Abeba	5.30	112.15	9.035	38.77	1998—2014
GUA	Guam	5.48	143.92	13.59	144.87	1991—2010
BNG	Bangui	4.1	91.52	4.33	18.57	1993—2011
DLT	Dalat	1.89	–179.32	11.95	108.48	2012—2014
HUA	Huancayo	–2.00	–3.05	–12.05	–75.33	2002—2016
ASC	Ascension Island	–2.52	57.06	–7.95	–14.38	2003—2014
GAN	Gan	–8.89	144.89	–0.6946	73.154	2012—2014
VSS	Vassouras	–13.43	27.06	–22.4	–43.65	1999—2014
PPT	Pamatai	–15.03	–74.53	–17.567	–149.574	1991, 1993—2014
API	Apia	–15.17	–97.02	–13.8155	–171.781	1999—2014
TSU	Tsumeb	–18.75	86.37	–19.202	17.584	2004—2014
IPM	Isla de Pascua Mataveri	–18.93	–34.72	–27.1713	–109.42	2010—2014
KDU	Kakadu	–21.63	–154.00	–12.686	132.47	2000—2014
PIL	Pilar	–21.61	7.63	–31.667	–63.881	2012—2014
CKI	Cocos-Keeling Islands	–21.90	168.45	–12.1875	96.8336	2013—2014
TAN	Antananarivo	–23.51	116.34	–18.917	47.552	1993—2008
KMH	Keetmanshoop	–26.01	85.40	–26.541	18.11	2009—2014
HBK	Heartebeesthoek	–27.03	94.99	–25.883	27.707	1999—2014
CTA	Charters Towers	–27.64	–138.69	–20.09	146.264	2000—2014
TDC	Tristan da Cunha	–31.44	54.19	–37.067	–12.316	2009—2014
LRM	Learmonth	–32.00	–173.10	–22.22	114.1	2004—2014
ASP	Alice Springs	–32.50	–151.46	–23.762	133.883	1999—2014
TRW	Trelew	–33.15	5.95	–43.267	–65.383	2000—2014
HER	Hermanus	–33.91	84.66	–34.425	19.225	1995—2014
GNG	Gingin	–41.06	–171,00	–31.356	115.715	2012—2014
GNA	Gnangara	–41.48	–170.72	–31.78	115.947	1994—2013
PST	Port Stanley	–41.79	11.91	–51.704	–57.89	2003—2014
CNB	Canberra	–42.29	–132.82	–35.32	149.36	1991—2014
AMS	Amsterdam Island	–46.03	144.95	–37.796	77.574	1991—2014
EYR	Eyrewell	–46.83	–106.00	–43.474	172.393	1994—2014
CZT	Port Alfred	–51.12	114.11	–46.431	51.86	1991—2014
AIA	Argentine Islands	–55.19	5.86	–65.245	–64.258	2001—2014
PAF	Port-aux-Francais	–56.62	133.62	–49.353	70.262	1991—2014
MCQ	Macquarie Island	–59.7	–115.78	–54.5	158.95	2001—2014
MAW	Mawson	–73.08	111.61	–67.6	62.88	2005—2014
DRV	Dumont d'Urville	–74.11	–129.14	–66.67	140.01	1991—2014
CSY	Casey Station	–76.10	–175.38	–66.28	110.53	2010—2014
SBA	Scott Base	–78.94	–71.17	–77.85	166.762	1996—2014
DMC	Dome C	–84.04	–135.88	–75.25	124.167	2009—2014
VOS	Vostok	–88.36	173.26	–78.464	106.835	2013—2014

Appendix B. Synchronous records of 27 geomagnetic observatories

Synchronous records of 27 geomagnetic observatories of North America region covering geomagnetic latitudes from 87° to 21° northern latitude (their position can be seen in Fig. 7 and 8, exact coordinates — in Appendix A). Observatories are given in the order of geomagnetic latitude decreasing. Examples selected during a great magnetic storm and a very calm day.

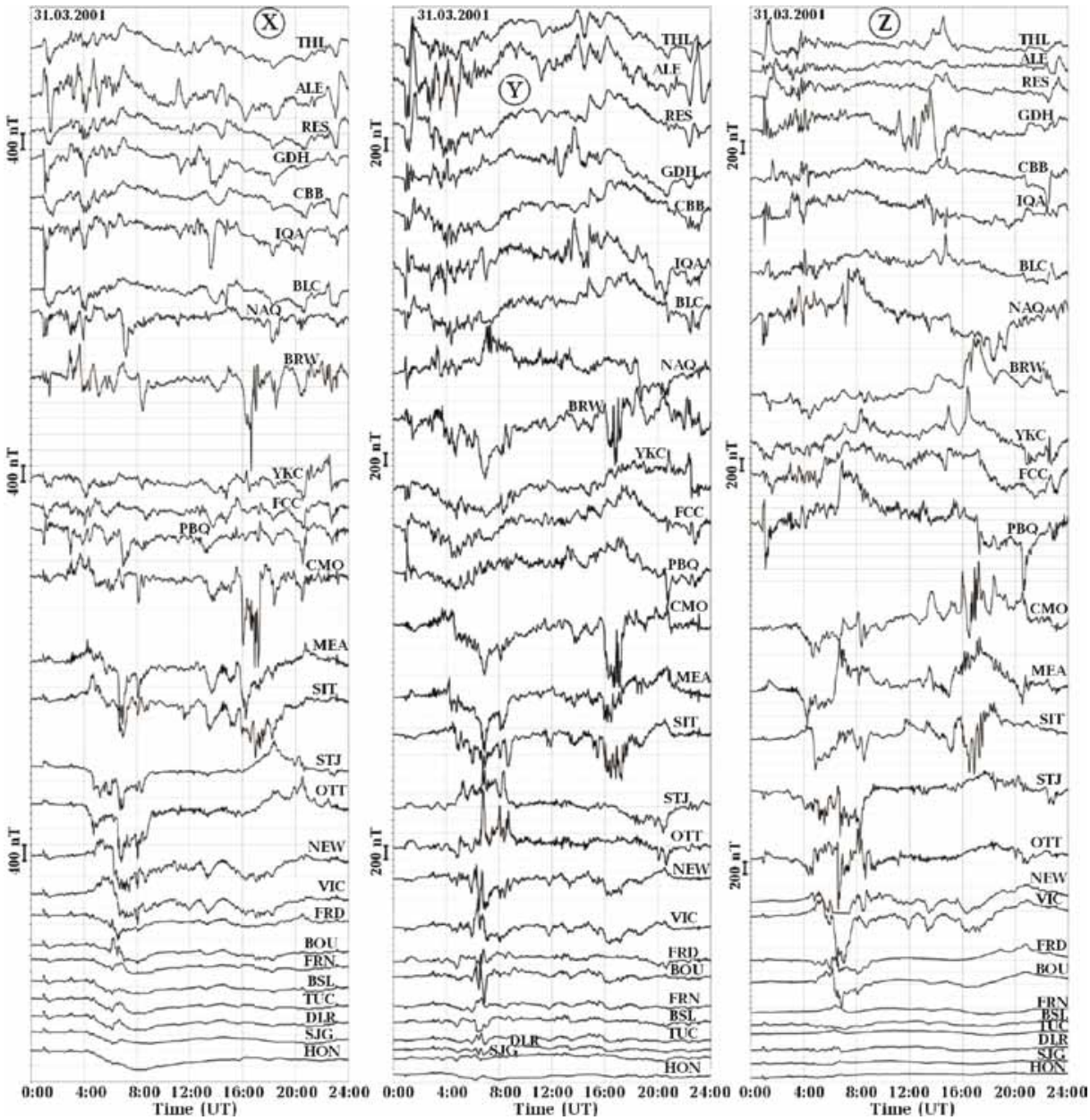

Fig. B1. Synchronous records of 27 geomagnetic observatories during great magnetic storm 31.03.2001 (with superimposed local substorms at high latitudes). K_p index of geomagnetic activity during the day varied for every 3-hour intervals as follows: 7–, 9–, 9–, 6+, 7, 8, 8+, 7+; the average for the whole day was 8–. Hours are marked in UT.

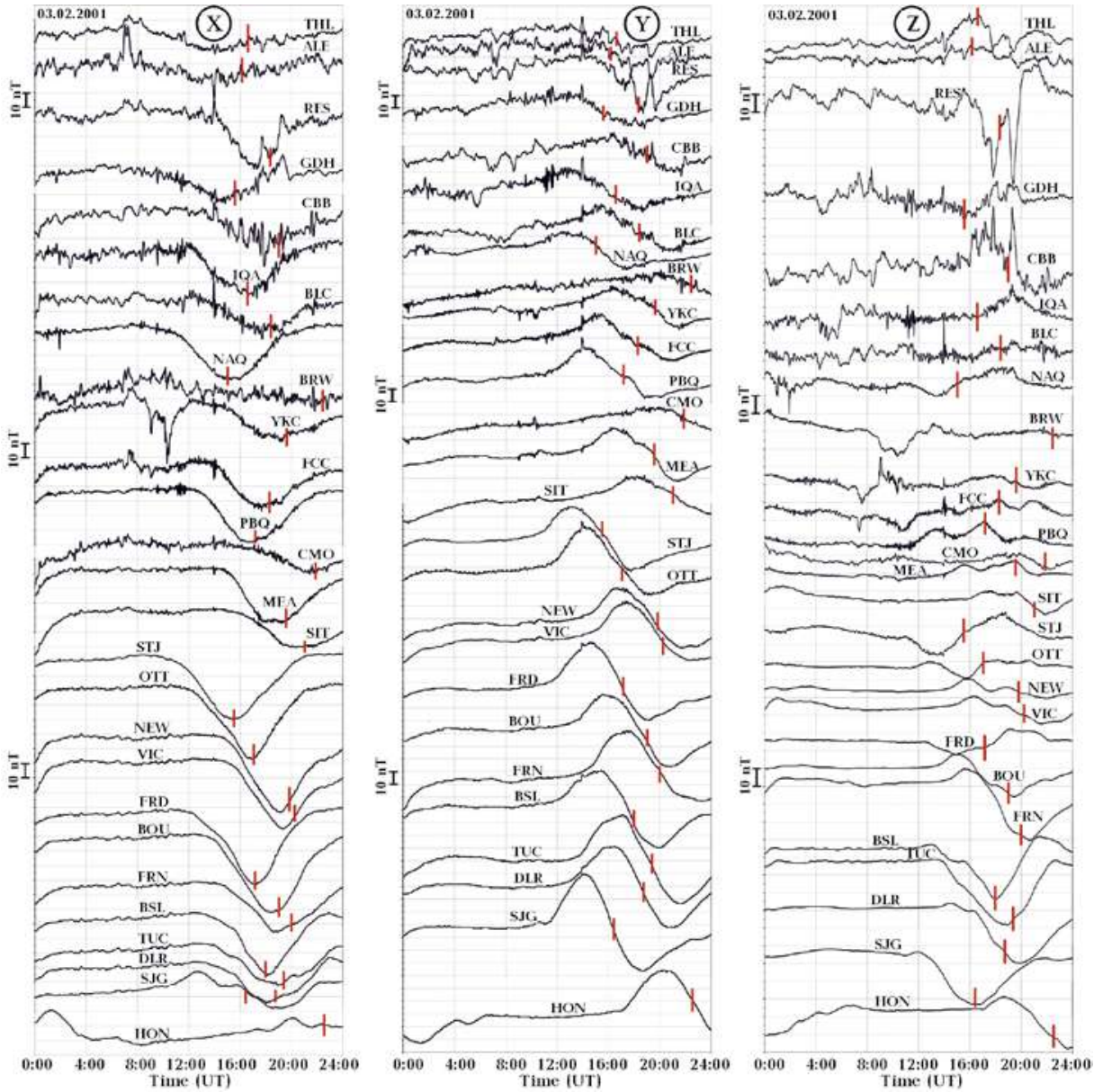

Fig. B2. Synchronous records of 27 geomagnetic observatories during a very calm day 3.02.2001. K_p index during the day varied for every 3-hour intervals as follows: 0+, 0, 0+, 0+, 1–, 0+, 0, 0. Short vertical lines mark midday for every observatory. Hours are given in UT.

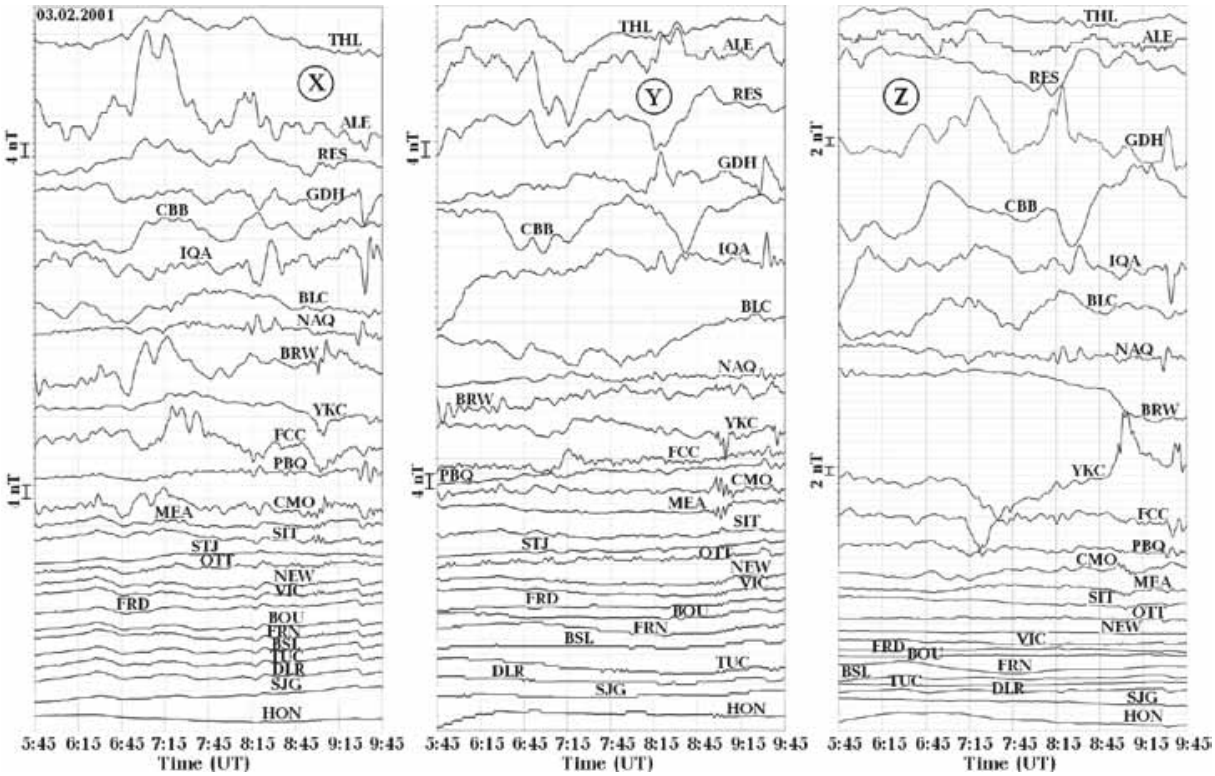

Fig. B3. Synchronous records of 27 geomagnetic observatories during 4 hours long fragment of Fig. B2 during local night when S_q-variation is minimal.

Appendix C. Induction arrow temporal variations at 32 North America observatories

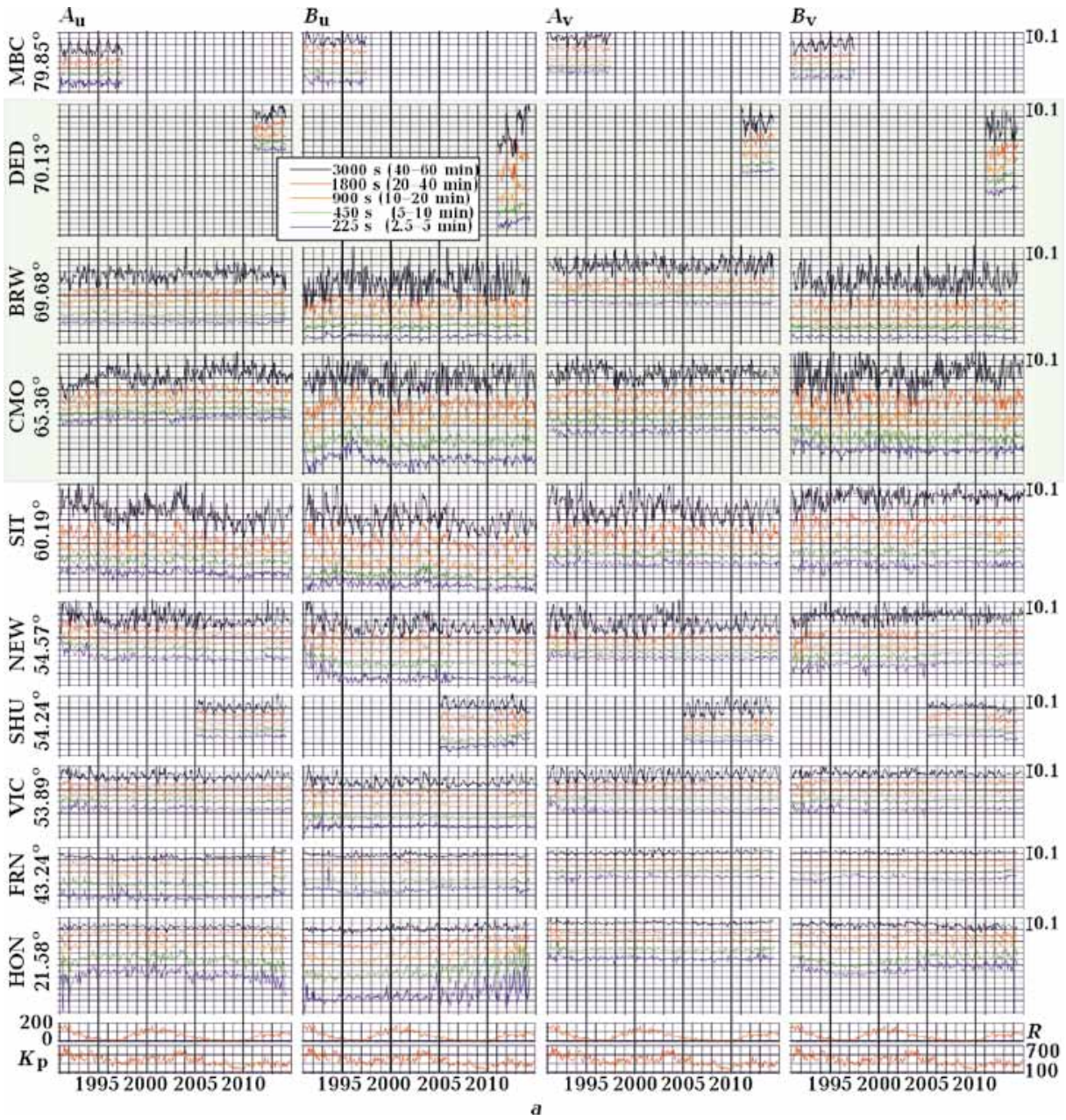

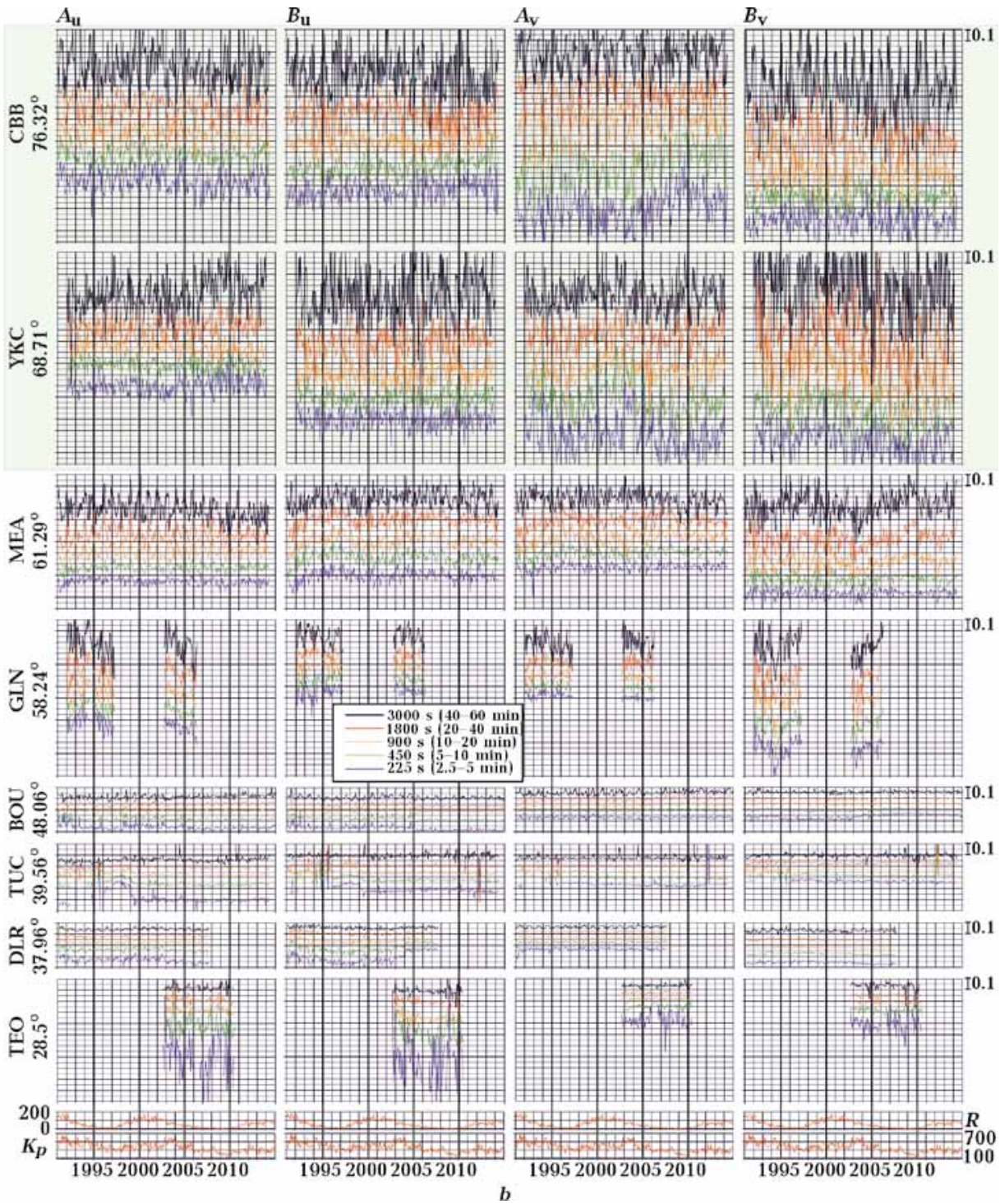
A_u
B_u
A_v
B_v
CBB 76.32°
YKC 68.71°
MEA 61.29°
GLN 58.24°
BOU 48.06°
TUC 39.56°
DLR 37.96°
TEO 28.5°
±0.1
3000 s (40–60 min)
1800 s (20–40 min)
900 s (10–20 min)
450 s (5–10 min)
225 s (2.5–5 min)
200
0
K_p
1995 2000 2005 2010
R
700
100

b

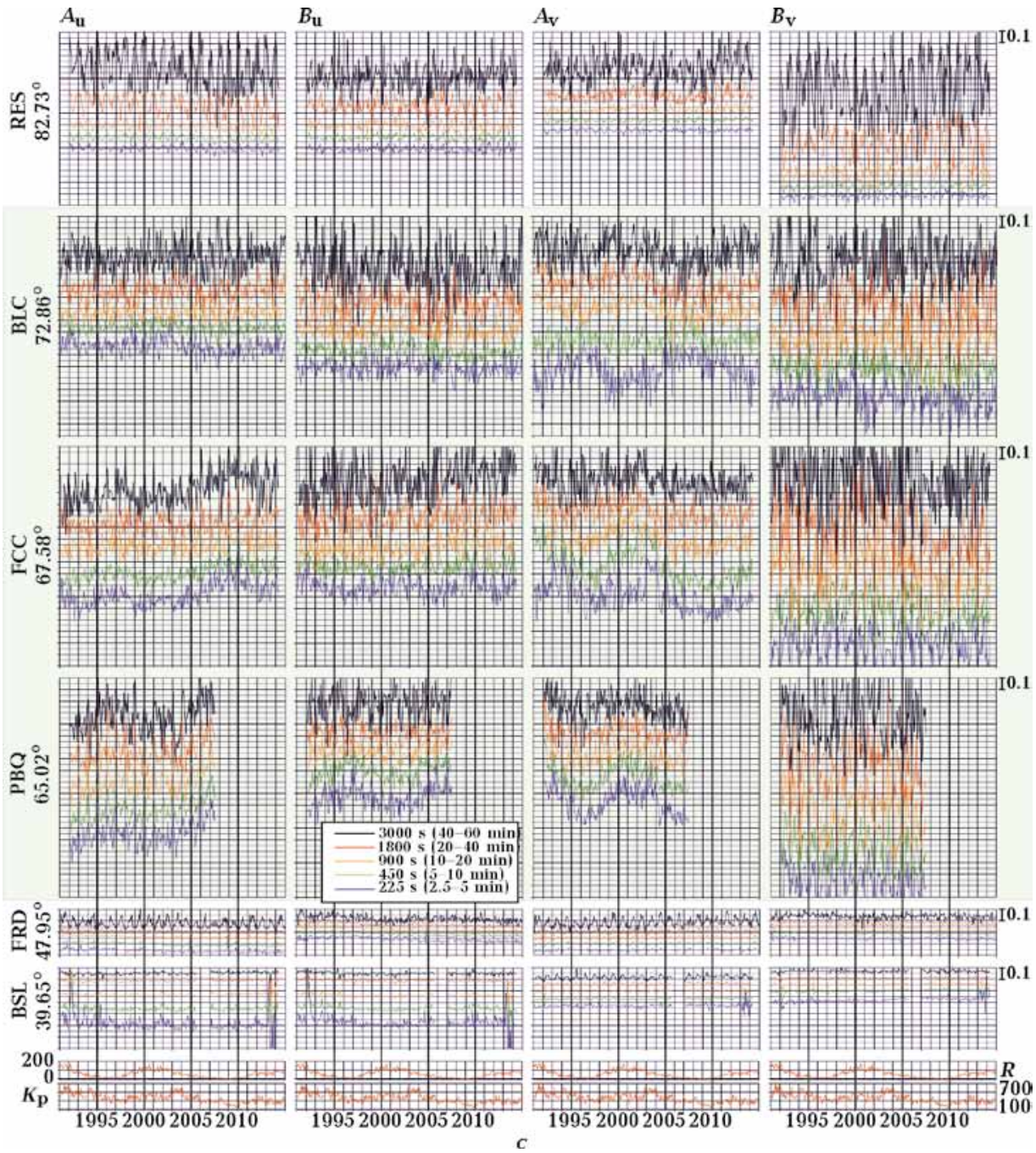
A_u
B_u
A_v
B_v
RES 82.73°
BLC 72.86°
FCC 67.58°
PBQ 65.02°
FRD 47.95°
BSL 39.65°
I0.1
3000 s (40–60 min)
1800 s (20–40 min)
900 s (10–20 min)
450 s (5–10 min)
225 s (2.5–5 min)
200
0
K_p
R
700
100
1995 2000 2005 2010

c

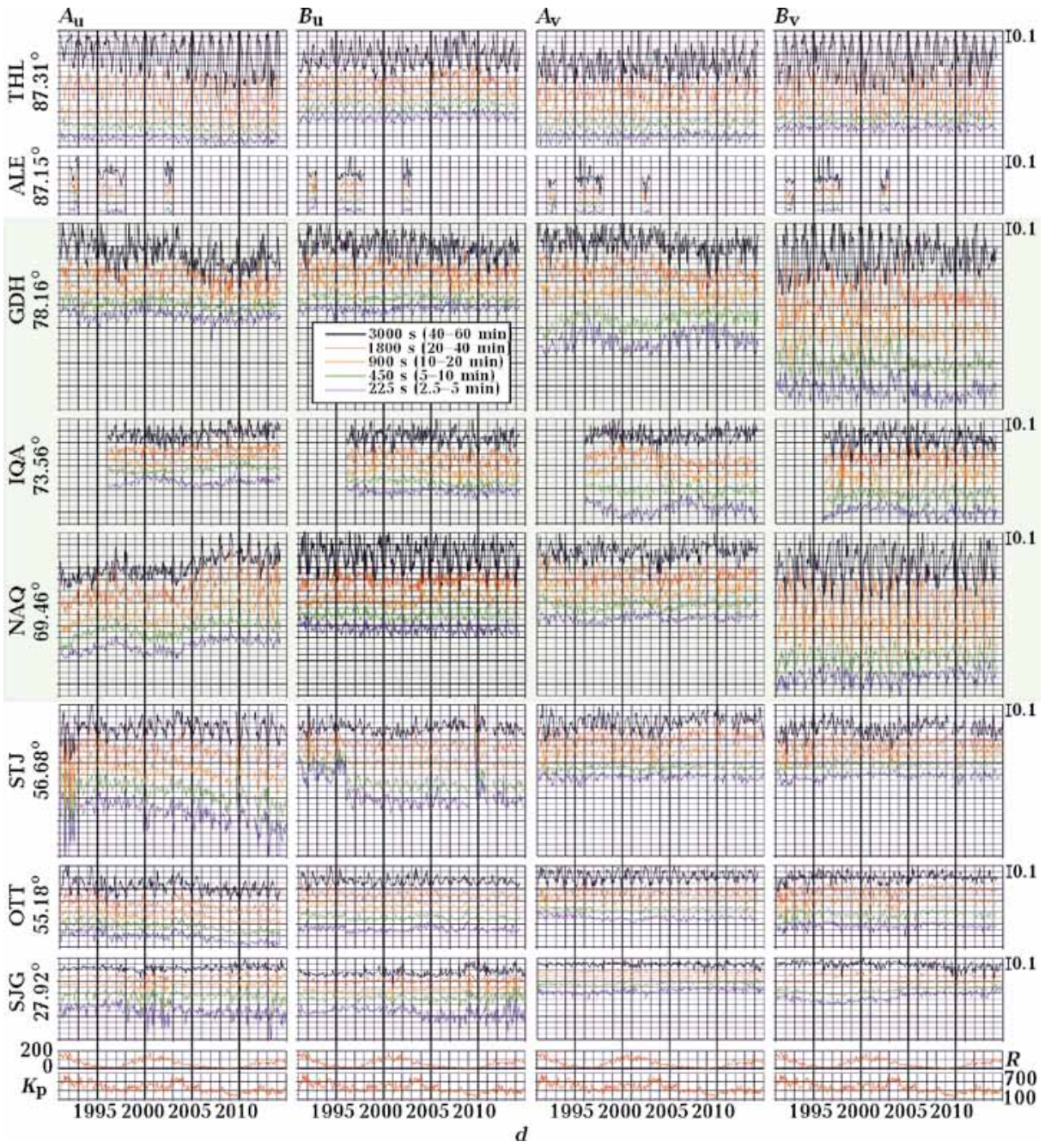

Fig. C1. Temporal variations of monthly mean values of induction arrow components A_u, B_u, A_v, and B_v for periods 3000 s, 1800 s, 900 s, 450 s and 225 s (given by different colors) during 1991—2014. Observatories disposed in 4 figures *a*—*d* according to geographical longitude and in every figure according to geomagnetic latitude. After each observatory code, geomagnetic latitudes for 2000—2010 epoch are given. Shaded background marks the observatories located in aurora zone (see Figs. 7 and 10). R is the index of solar activity (Wolf number), and K_p is the monthly sum of the planetary index of geomagnetic activity.

Appendix D. coherence and diurnal spectra at 34 North America region geomagnetic observatories

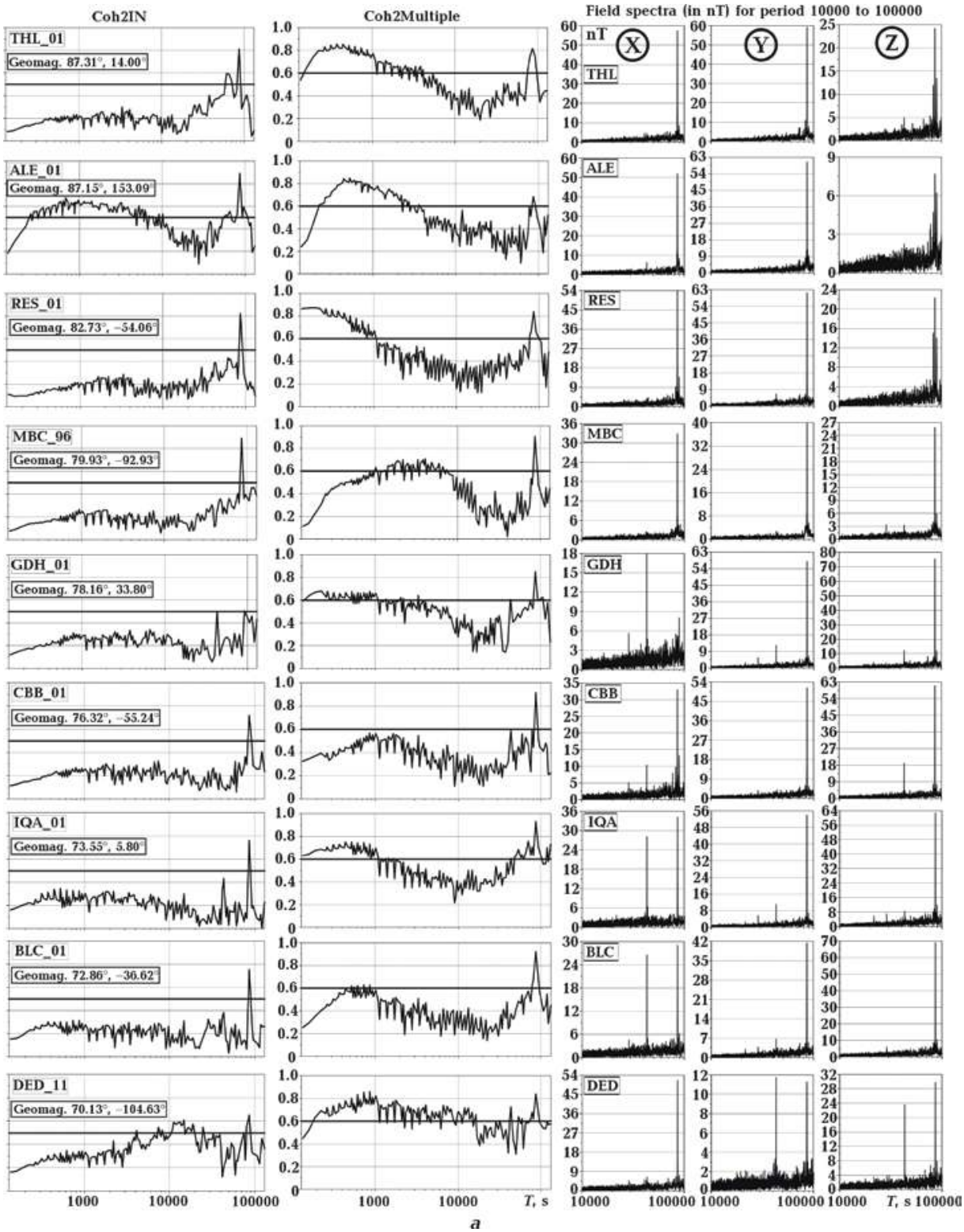

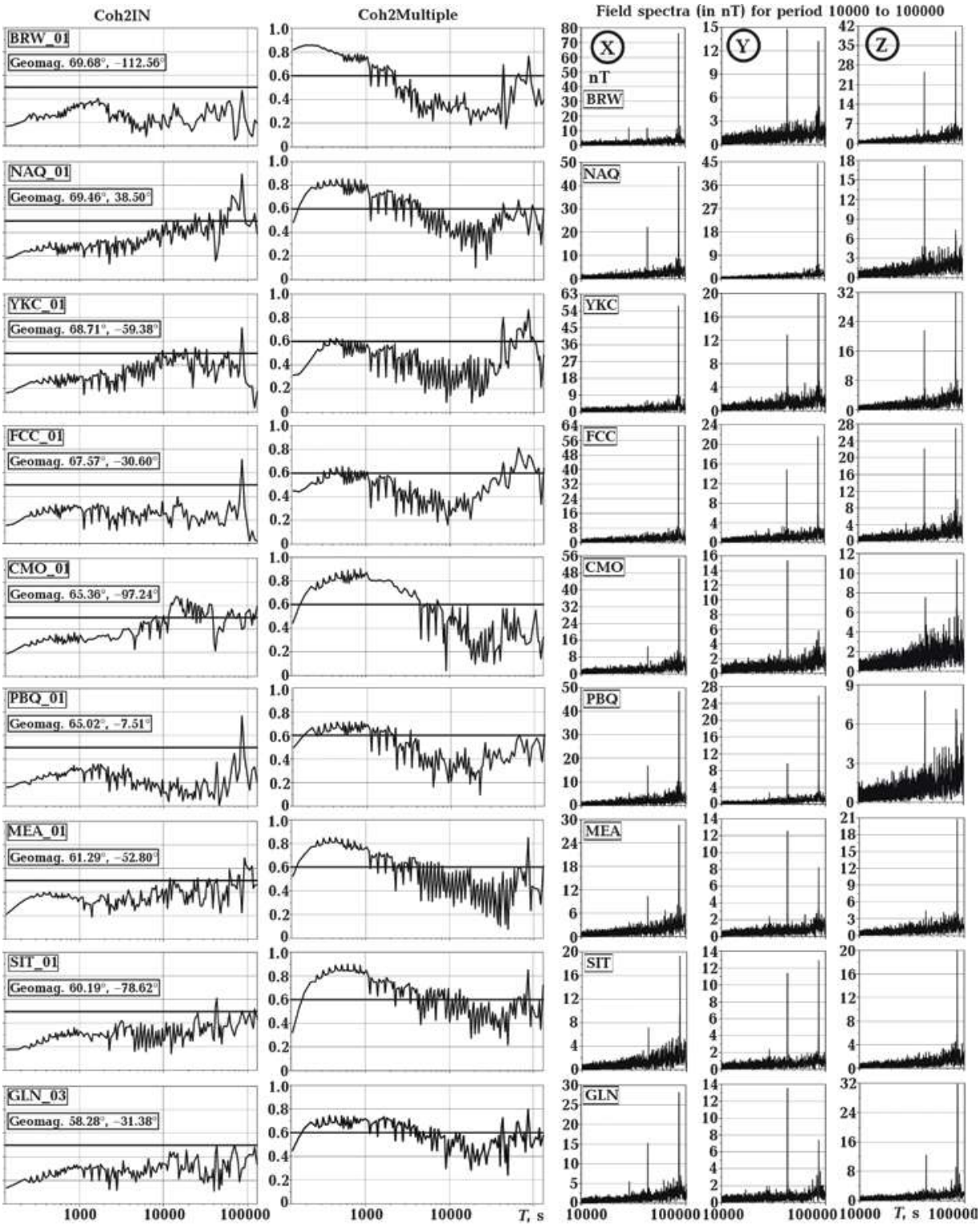
Coh2IN
Coh2Multiple
Field spectra (in nT) for period 10000 to 100000
BRW_01
Geomag. 69.68°, –112.56°
NAQ_01
Geomag. 69.46°, 38.50°
YKC_01
Geomag. 68.71°, –59.38°
FCC_01
Geomag. 67.57°, –30.60°
CMO_01
Geomag. 65.36°, –97.24°
PBQ_01
Geomag. 65.02°, –7.51°
MEA_01
Geomag. 61.29°, –52.80°
SIT_01
Geomag. 60.19°, –78.62°
GLN_03
Geomag. 58.28°, –31.38°
X
Y
Z
nT
BRW
NAQ
YKC
FCC
CMO
PBQ
MEA
SIT
GLN
1000
10000
100000
T, s

b

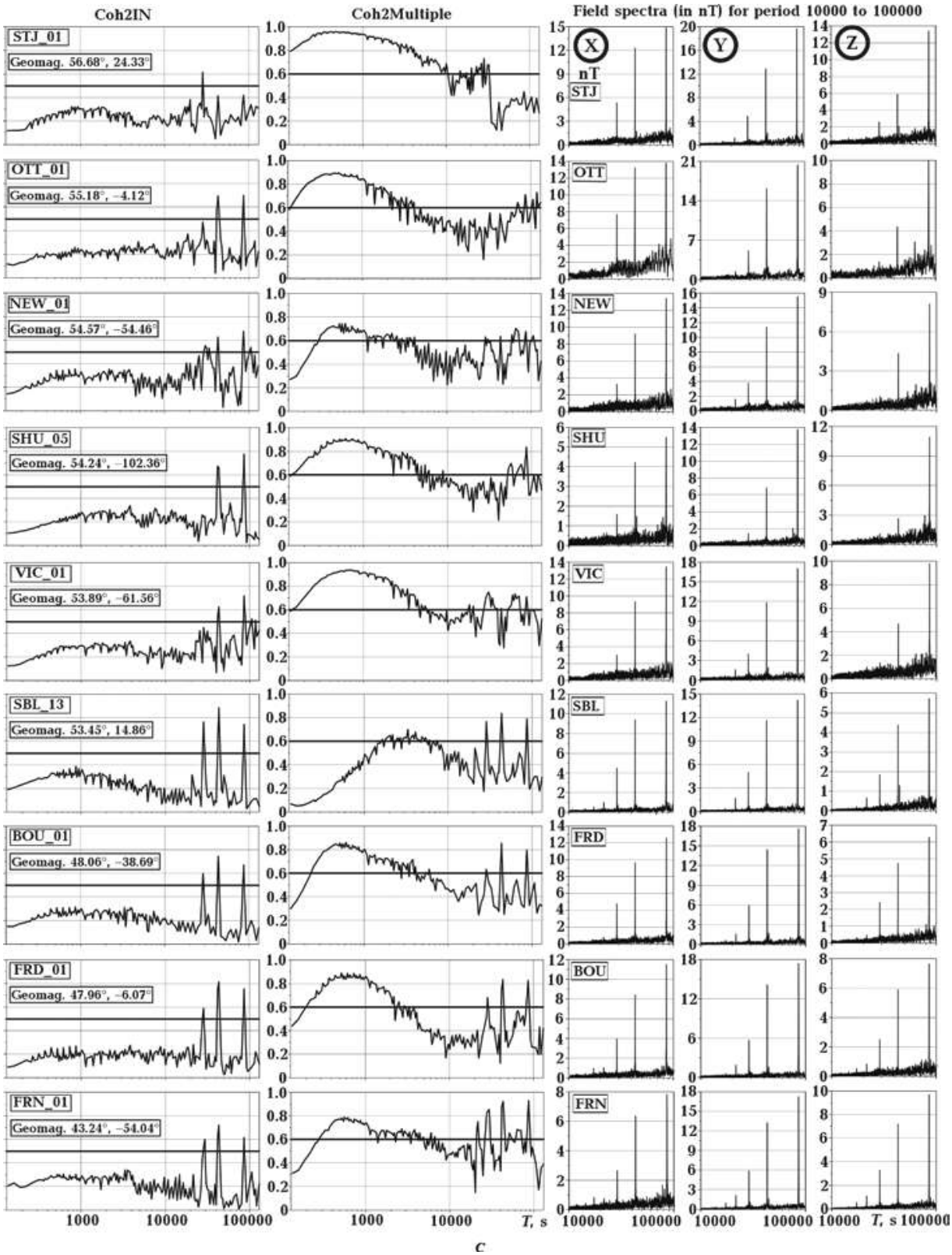
Coh2IN
Coh2Multiple
Field spectra (in nT) for period 10000 to 100000
STJ_01
Geomag. 56.68°, 24.33°
OTT_01
Geomag. 55.18°, –4.12°
NEW_01
Geomag. 54.57°, –54.46°
SHU_05
Geomag. 54.24°, –102.36°
VIC_01
Geomag. 53.89°, –61.56°
SBL_13
Geomag. 53.45°, 14.86°
BOU_01
Geomag. 48.06°, –38.69°
FRD_01
Geomag. 47.96°, –6.07°
FRN_01
Geomag. 43.24°, –54.04°
X
Y
Z
nT
STJ
OTT
NEW
SHU
VIC
SBL
FRD
BOU
FRN
1000
10000
100000
T, s

c

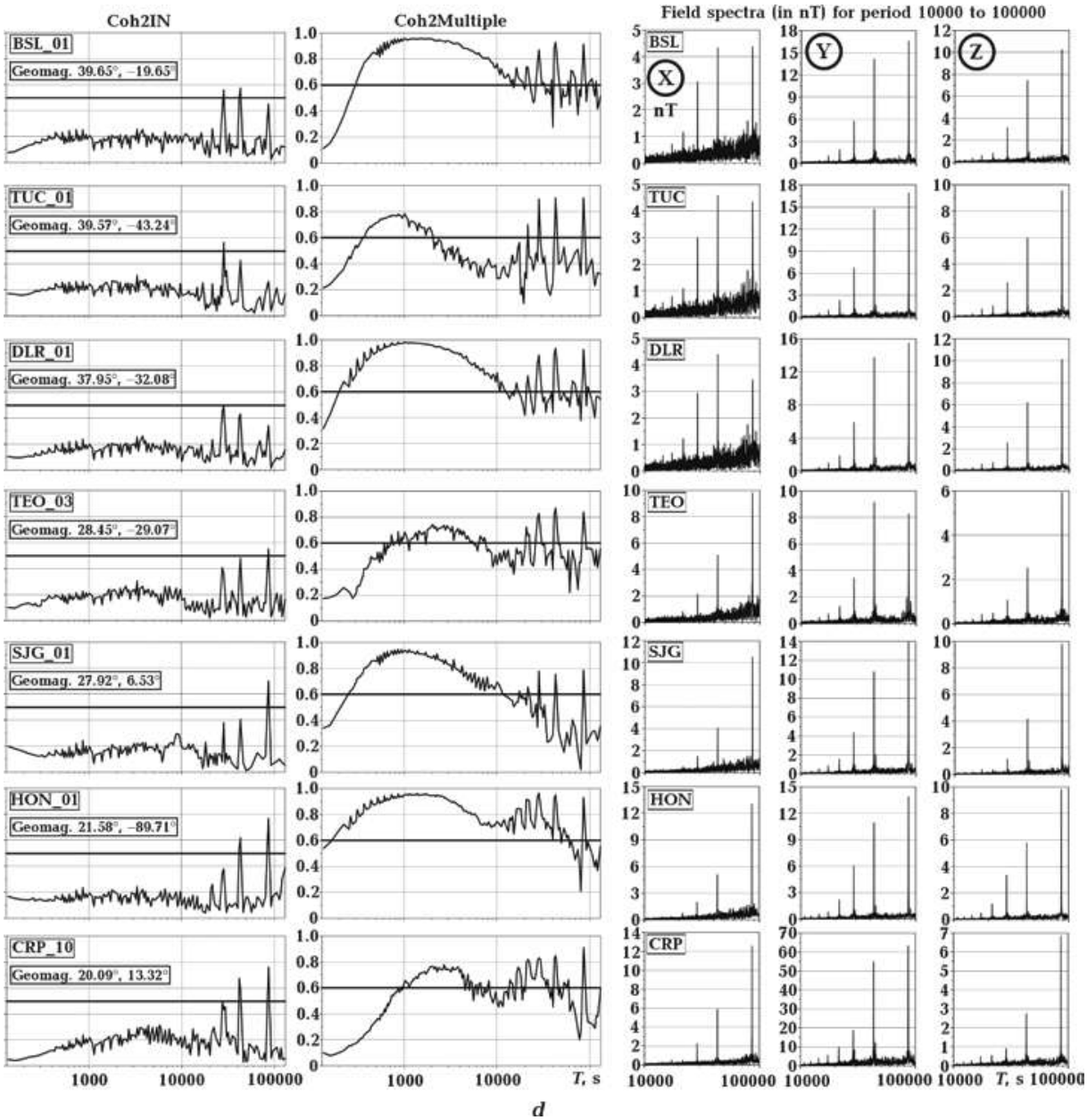

Fig. D1. Squared input and multiple coherences mainly for the whole 2001 year (two numbers after observatory code mark the year used) in period interval 200—100000 s and spectral density in nT of geomagnetic field components in period interval 10000—100000 s at 34 North American, Greenland and Hawaii (shortly North American region) observatories presented in order of geomagnetic latitude diminishing.